Title
Electronic Structure of Novel Materials for Next-Generation Devices

Author
Shearer, Alex J.

Publication Date
2016

Peer reviewed|Thesis/dissertation

Electronic Structure of Novel Materials for Next-Generation Devices

by

Alexander Jacques Shearer

A dissertation submitted in partial satisfaction of the

requirements for the degree of

Doctor of Philosophy

in

Chemistry

in the

Graduate Division

of the

University of California, Berkeley

Committee in charge:

Professor Charles B. Harris, Chair
Professor Martin Head-Gordon
Professor Michael F. Crommie

Spring 2016

Electronic Structure of Novel Materials for Next-Generation Devices

Abstract

Electronic Structure of Novel Materials for Next-Generation Devices

by

Alexander Jacques Shearer

Doctor of Philosophy in Chemistry

University of California, Berkeley

Professor Charles B. Harris, Chair

The properties of interfacial electronic states in device-relevant materials are investigated using time- and angle-resolved two photon photoemission (TPPE) spectroscopy.

Angle- and time-resolved TPPE is used to investigate electronic states in the buffer layer of 4H-SiC(0001). An image potential state (IPS) series is observed on this strongly surface-bound buffer layer, and dispersion measurements indicated free-electron-like behavior for all states in this series. These results are compared with TPPE taken on bilayer graphene, which also shows the existence of a free-electron-like IPS series. Lifetimes for the n = 2, and n = 3 states are obtained from time-resolved TPPE; slightly increased lifetimes are observed in the bilayer graphene sample for the n = 2 the n = 3 states. Despite the large band gap of graphene at the center of the Brillouin zone, the lifetime results demonstrate that the graphene layers do not behave as a simple tunneling barrier, suggesting that the buffer layer and graphene overlayers play a direct role in the decay of IPS electrons.

Ultrafast response of the room temperature ionic liquid (RTIL) 1-butyl-1-methyl- pyrrolidinium bis(trifluoromethylsulfonyl)imide ([Bmpyr][NTf_2]) to a photoinjected electron is investigated in few-monolayer films using time- and angle-resolved two-photon photoemission spectroscopy. A delocalized precursor state and a localized solvated state are resolved at early times, but after 200 fs only a single solvated state is observed. The dynamics of film response to this solvated state are shown to depend significantly on film temperature and thickness. Population lifetime measurements demonstrate that the RTIL film can significantly affect the coupling between solvated state and metal substrate, as the solvated state's average lifetime increases from 90 ± 20 fs in 1 ML films to 195 ± 83 ps in 3 ML films. Additionally, a temperature dependence of the time-dependent binding energy shift of the solvated state after c.a. 500 fs is attributed to a phase change occurring between the two temperature regimes that were investigated. Results from xenon overlayer experiments suggest that the solvation process occurs near the surface of the RTIL film. Finally, film degradation is found to be present, suggesting that the observed solvation response could involve a radical species.

Valuable information about two very different interfacial materials is collected using TPPE, proving the power and versatility of the technique. The results presented here show that interfacial states can be used to monitor a variety of physical phenomena, from corrugation in graphitic materials to solvation and degradation in RTILs.

I dedicate this work to my parents Elizabeth and Michael and to my brother Samuel.
Through all of life's challenges, you have always been there for me.

Contents

List of Figures

List of Tables

Acknowledgments

During my time in the Harris group, I was fortunate enough to work with a uniquely supportive group of young scientists that made the marathon of graduate school feel like a race worth running.

Eric Muller and Ben Caplins were both pivotal to my development during graduate school. Eric and Ben are not only technically brilliant but are also thoughtful, patient, and both highly value the teaching process. I have very little doubt that both Eric and Ben will continue on to be excellent scientists, and I hope that others will benefit from their teaching in the way that I have.

David Suich and I started at the same time in the Harris group 6 years ago, but it was only within the last 6-8 months that I started to really appreciate how lucky I've been to learn alongside with such a smart, hardworking, and humble person.

I want to specially acknowledge one of the most successful Harrisites and a personal friend, Justin Lomont, as one of my favorite people from Berkeley. Justin is another scientific superstar who, despite his unbelievably impressive accomplishments, maintains a down-to-earth personality, outlandish sense of humor, and is one of the kindest people I've ever been fortunate enough to meet.

Kathleen Fowler was kind of like a second parent out in California. Kathleen always knew how to make me laugh, gave sound advice, and guided me though more than one maze of paperwork. In between long hours in the lab, it was always great to have someone to chat with and whose dog happened to be adorable.

I conclude by thanking my advisor, Charles, for supporting me for the last 6 years. Perhaps some of the most enriching experiences of my graduate career have come from presenting at conferences, two of them international meetings in Japan. I have Charles to thank for allowing me to attend these conferences on the group's behalf, supporting me financially, and preparing me to present my work to the international community. I finally want to thank Charles for being so supportive as I make the career jump from physical chemistry to a technical role at a data-driven company in the San Francisco area.

This work was supported by the Director, Office of Energy Research, Office of Basic Energy Sciences, Chemical Sciences Division of the U.S. Department of Energy, under Contract No. DE-AC02-05CH11231.

Chapter 1

Introduction

1.1 Interfaces of Novel Materials

The chemistry and physics that occurs at interfaces is important to understand for a wide variety of applications. There are countless examples of how devices rely on, or can be improved by, understanding the processes that occur at the interface between dissimilar materials. Devices such as Li^+ batteries, electrochemical capacitors, organic photovoltaics, and trace gas sensors all benefit from processes occurring at interfaces. In the case of these examples, there are traditional methods for constructing each device using materials whose interfacial structure and behavior has been well-known for many decades. The purpose of this dissertation is to discuss the interfacial behavior of two types of novel materials, whose interfacial characteristics and potential real-world impact have only begun to be explored in recent years. The two materials that will be discussed are graphene, a 2-dimensional sheet of carbon atoms arranged in a honeycomb-like structure, and room temperature ionic liquids (RTILs), organic salts whose bulky and asymmetric structure allows them to exist as liquids under ambient conditions.

Graphene

Graphene is a 2-dimensional sheet of sp^2-hybridized carbon atoms bonded together in a hexagonal, honeycomb arrangement. Single-layer samples of graphene were isolated at Manchester University in 2004 [62]. Graphene samples have facilitated the observation of physical phenomena such as the ambipolar field effect [62], room temperature quantum Hall effect [63], and relativistic charge carrier speeds [61]. Though the lack of a scalable synthesis procedure has prevented the widespread use of graphene in devices, there have been exciting studies that show how powerful graphene can be when incorporated into a device. For example, it was shown that graphene can be used to build a gas sensor that can detect the adsorption of single molecules [71]. Advantages that graphene holds over other materials used in traditional sensors are its 2-D structure and subsequently maximized surface area,

high conductivity, and low Johnson noise. These characteristics highlight the importance of interfacial properties, as they are all linked to the surface-only physical structure of graphene.

Graphene can be obtained by mechanical exfoliation techniques [62], but there are important advantages to alternative methods of preparation. For example, simply heating a silicon carbide (SiC) substrate leads to the carbon within the SiC forming sheets of graphene [42]. This growth process can be carefully controlled by tuning the annealing procedure, and this process leads to graphene samples formed on a substrate with a device-suitable band gap and no need for an external carbon source. Using SiC as the substrate for graphene is convenient with respect to the synthesis and device construction process, but it has also been shown that this substrate can improve the actual performance of devices. For example, using SiC reduces the noise in graphene systems, leading to improved performance in high-speed electronic devices [54]. Graphene has facilitated many interesting results, but there is still much to learn about this unique material and its interfacial behavior. The present work focuses on graphene and its interfacial behavior on the device-relevant substrate SiC.

Room Temperature Ionic Liquids

The history of RTILs extends back to the early 20th century. One of the first publications on RTILs dates back to 1914, where physical properties of ethylammonium nitrate were studied [91]. The field of RTILs was restricted mostly to specialists until 2000, when interest in industrial applications of RTILs was rekindled after an Advanced Research Workshop held by NATO [66, 14]. This conference was a turning point in the field; researchers began to realize the potential impact of RTILs in an industrial context, leading to a resurgence of interest in these compounds.

Properties such as high electrochemical stability, low vapor pressure, non-flamability, and ionic conductivity make RTILs attractive for use in devices because they are able to both improve device performance and make the device safer to produce and use. In addition, a great advantage of RTILs is that they afford a high degree of tunability. Substituting different cations or anions allows for specific properties of RTILs to be tuned. Since pairing all possible RTIL cations and ions yields more than 10^6 possible compounds [66], it is highly likely that there is a suitable RTIL for most applications. The difficulty is not a lack of options, it is understanding the trends in structure and function of RTILs and therefore knowing where to look.

A large amount of work has been done, mostly since the year 2000, to study the properties of RTILs and establish links between structure and behavior. There are several excellent reviews that thoroughly outline the many modern studies of RTILs [15, 14, 34, 66]. An immense amount of insight has been gathered in the last 15 years, with the majority of the studies focusing on bulk properties and behavior. In the context of electrochemical devices, it is extremely important to understand the surface properties of RTILs because, as noted earlier herein, interfacial properties often influence or even dominate the performance of devices. There have been some studies of RTILs at interfaces, one review even specifically focuses on electrified interfaces relevant to electrochemical devices [27]. What was not shown

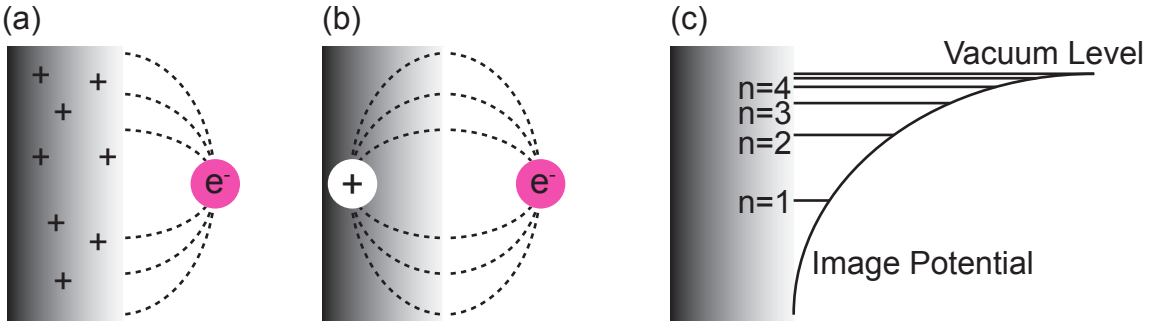

Figure 1.1: A negative electron positioned near the metal surface induces a polarization within the material, shown in (a). The resulting polarization can be represented as a positive charge of equal magnitude within the metal, shown graphically in (b). This method of solving the electrostatic problem of an electron outside a conductive surface is known as the method of images, and gives rise to an attractive potential known as the image potential. The image potential and Rydberg series of states it gives rise to are shown in (c).

until recently, however, was the behavior of an interfacial RTIL on the ultrafast ($<10^{-12}$ second) timescale [55]. The present work outlines an expansion of the first ultrafast study of an interfacial RTIL. The behavior of a specific compound, 1-Butyl-1-methylpyrrolidinium bis(trifluoromethanesulfonyl)imide ([Bmpyr][NTf_2]), is shown - but perhaps more importantly, two-photon photoemission (TPPE) is showcased as a powerful tool for use in the RTIL community.

1.2 Image Potential States

A charge placed a distance z outside of a conductive surface induces a polarization of charges within the material. Solving the appropriate differential equation gives a result equivalent to having a charge of equal magnitude but opposite sign at a distance -z within the material. The resulting potential is known as the image potential, and is proportional to 1/z outside the material. The image potential gives rise to a Rydberg series of surface states which, similar to the case of a hydrogen atom, are indexed by the quantum number n and converge toward the vacuum level as n$\rightarrow \infty$. For the case of a clean metal, the energies are given by Equation 1.1:

$$E_n = \frac{-0.85eV}{(n+a)^2} + V_0 \tag{1.1}$$

These so-called image potential states are inherently bound to the surface, and can serve as sensitive probes of many interfacial phenomena. The image potential and series of Rydberg states are shown in Figure 1.1(c). The typical distance of the n = 1 IPS electron density from a clean metal is 3 Å, while the same distance for the n = 2 is 10-12 Å. Though bound in the surface-normal direction, IPS's of a clean metal surface are typically free-electron-like

in the plane of the surface. This is based on the assumption that while an IPS electron experiences the image potential in the surface normal direction, the potential in the plane of the surface is flat. The parallel energy of the electron is given by:

$$E_{||} = \frac{\hbar^2 k^2}{2m_e} \tag{1.2}$$

Momentum-resolved experiments can shed light on whether a state is delocalized or localized by observing the curvature of a band. As will be discussed later, there are many cases where surface electronic states become localized.

1.3 Two-Photon Photoemission Spectroscopy

Two-photon photoemisson spectroscopy can be used to interrogate both occupied and unoccupied electronic states at metal or molecule-metal interfaces. The surface sensitivity, ability to measure band structure, and femtosecond temporal resolution of this technique make TPPE an ideal tool for studying interfacial states in device-relevant materials.

The TPPE process is graphically outlined in Figure 1.2. A femtosecond laser pulse with energy $h\nu_1$ is used to initiate the TPPE process. This pulse serves as a pump pulse: it excites an electron into a previously unoccupied energy level, which is referred to as an *intermediate state*. After a variable waiting time τ, a second pulse is introduced with energy $h\nu_2$. This second pulse acts as the probe pulse: it excites the population of the intermediate state to a continuum level above the vacuum level of the system. The kinetic energy of the free-electron final state is measured by a time-of-flight detector. The intermediate state energy can be determined by subtracting the known energy of the probe pulse ($h\nu_2$) from the measured final state's kinetic energy. Since the waiting time τ between pump and probe can be varied on the femtosecond timescale, the ultrafast evolution of surface states can be monitored using TPPE.

The work function of a sample is an important measurement in most studies, and can be obtained directly by TPPE by two possible methods. The first method is to systematically vary the energy of the probe pulse $h\nu_2$ over a range near the estimated work function of the sample. The onset of single-photon photoemission is used in this case to measure the work function of the sample. A second option is to use the signal collected from nonresonant excitations. The high energy cutoff of the nonresonant background is equal to the Fermi energy plus the energies of pump ($h\nu_1$) and probe ($h\nu_2$) pulses. The low energy cutoff is simply equal to the vacuum level, so the difference between the two cutoffs gives a good approximation of the sample work function.

Angle resolving TPPE measurements yields information on the spatial localization of surface electronic states. The present setup allows for the measurement of the parallel component of a photoemitted electron's wavevector via simply rotating the sample relative to the fixed detection point, as shown in Figure 1.2(b).The detector-sample angle and the

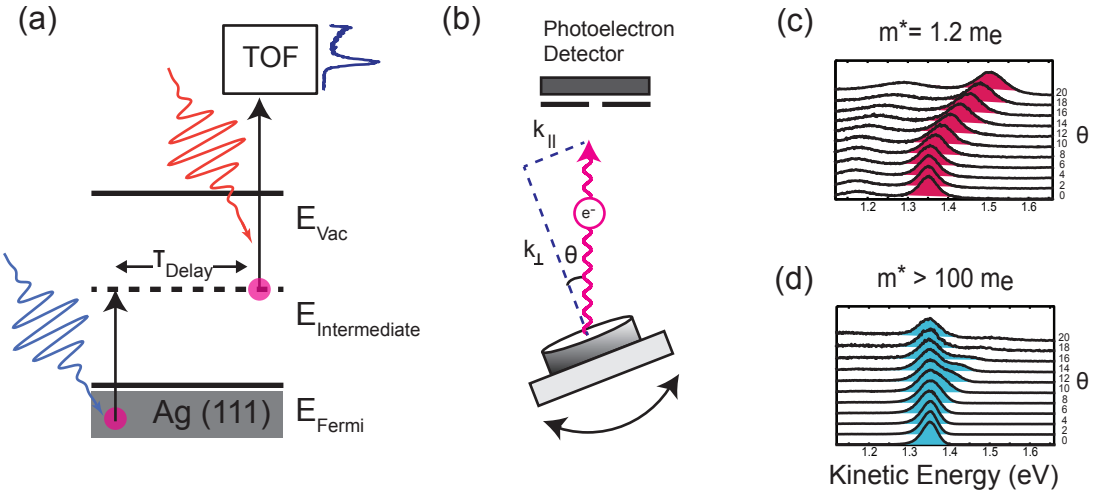

Figure 1.2: (a) The TPPE process is initiated by a pump pulse that excites an electron into an intermediate state. After a variable time delay, a probe pulse photoemits the electron and its kinetic energy is measured by a time-of-flight detector. Spectra can be collected for different values of parallel momentum $k_{||}$ by varying the detector angle, as shown in (b). Delocalized states are characterized by an effective mass m^* of $\sim$1 and a measured kinetic energy that varies parabolically with the detection angle θ, (c) shows an example of results from delocalized state. An $m^* >> 1$ indicates a localized state with a flat band, whose kinetic energy is constant with changing angle. An example of spectra collected for a localized state is shown in (d).

photoemitted electron's parallel momentum $k_{||}$, energy $E_{photoemitted}$, and effective mass m^* are all interrelated via Equation 1.3.

$$k_{||} = \sqrt{\frac{2 \cdot m_e \cdot E_{photoemitted}}{\hbar^2}} \cdot sin\theta \tag{1.3}$$

A series of TPPE spectra can be collected at a series of different angles, then the movement of peaks in the energy domain can be used to determine the localization of the corresponding states. Examples of this type of experiment are shown in Figure 1.2 (c) and (d). In Figure 1.2(c), the peak energy shifts in an approximately parabolic pattern as the angle is increased. This is indicative of a free-electron-like delocalized state, and is described by an effective mass $m^* \approx 1$. In contrast, Figure 1.2(d) shows a series of spectra where the kinetic energy of the state is constant as a function of angle. This situation is indicative of a state localized in the surface plane, and is described by an effective mass $m^* >> 1$.

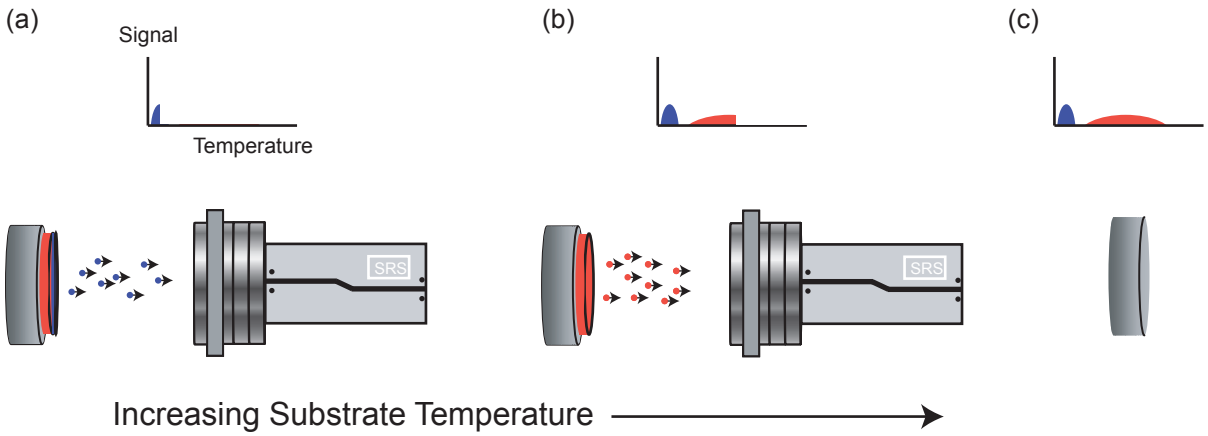

Figure 1.3: In a temperature programmed desorption experiment, the film temperature is slowly ramped, allowing coverages with dissimilar affinities for the substrate to desorb. Panel (a) is a cartoon of early in a TPD experiment, where there is insufficient thermal energy to desorb a strongly bound monolayer (orange) but sufficient energy for a weakly bound multilayer (blue) to desorb. As the temperature is increased, the strongly bound monolayer will desorb, as depicted in (b). The final result, shown in (c), is complete desorption of both coverage regimes, leading to two peaks in the TPD spectrum.

1.4 Measuring Film Coverage

Temperature programmed desorption (TPD) was used to characterize the coverage regime of adsorbates, specifically RTIL films. In a TPD experiment, the signal acquired by a mass spectrometer at a particular m/z ratio is tracked as a function of film temperature. As the temperature is increased, the thermal energy of the system approaches and exceeds the strength of the adsorbate/substrate binding interaction, and molecules begin to desorb. In the case of a single-coverage system, a TPD spectrum would result in a single peak. However, in the case of a multiple-coverage system where the adsorbate coverages have different affinities for the substrate, multiple peaks can be resolved as molecules from the different coverage regimes will desorb at different temperatures.

Figure 1.3 shows a cartoon example of what a TPD experiment would look like for a generic two-coverage system. The blue shaded regions represents a weakly-bound overlayer, while the orange shaded regions represent a strongly bound monolayer. At low temperatures, there is only enough thermal energy to desorb the weakly-bound overlayer, and a single peak develops. As the temperature is increased, the strongly-bound monolayer begins to desorb, leading to the final spectrum shown in 1.3(c).

Chapter 2

Experimental

2.1 Ultrafast Laser System

Pump Laser

Ultrafast pulses used to perform these experiments are generated by commercial Coherent Inc lasers. A solid state pump laser (Verdi V-18) with continuous wave output at 532 nm is used to pump a femtosecond oscillator (Mira 900) and regenerative amplifier (RegA 9000). A beam splitter directed 1/3 (6W) of the pump laser's total power (18W) to the oscillator, while the remainder of power (12W) was used to pump the regenerative amplifier. The only modification made to the pump laser in the last 5 years was the replacement of a diode and the laser head, after a campus-wide power surge caused these parts of the equipment to fail. It is possible to use two pump lasers to power the oscillator and amplifier separately. This was done prior to the start of these studies for a number of years; a V5 Verdi supplied 5 W to the oscillator while a V10 Verdi supplied 10 W to the amplifier. For all of the experiments described in this dissertation, however, the split output of the Verdi V18 was used to pump the oscillator and regenerative amplifier.

Pulse Generation

In the Mira 900, 532 nm light from the Verdi pump laser is converted into femtosecond pulses that are emitted at a repetition rate of 76 MHz. A starter assembly is used to modulate the length of the lasing cavity, this process initiates Kerr-lens mode locking which ultimately leads to the formation of femtosecond pulses. A prism pair and folding mirror are used to compensate for dispersion. Mode locking can be monitored by a 400 MHz oscilloscope and a fast photodiode mounted inside the laser. Optimal operating conditions lead to the Mira 900 generating pulses centered at 800 nm (ca. 10 nm fwhm) with pulse energies of around 12 nJ and repetition rate of 76 MHz. The spectrum of the output is monitored using an Ocean Optics spectrometer, the center wavelength and bandwidth would often slowly drift over the

course of 6-8 months. The Mira is realigned every ∼6 months to maintain its optimal output at 800 nm with 10 nm fwhm.

Pulse Amplification

In order to generate visible and UV pulses appropriate for TPPE, the 12 nJ output of the Mira 900 needs to be amplified. The 76 MHz output of the Mira is directed into the RegA 9000, where pulses are selected and amplified by a factor of 10^3. Injection of pulses from the oscillator is performed using an acousto-optic crystal. Amplification occurs over the course of 20-25 cavity round trips, after which the amplified pulse is ejected using a second acousto-optic crystal. The typical repetition rate for the RegA's output is 300 kHz.

Generating Visible Pulses

The final stage of the commercial laser system, the optical parametric amplifier (OPA) converts the 800 nm μJ pulses emitted by the RegA 9000 into visible light with pulse energies of around 67 nJ. The OPA functions by converting a portion of the RegA's 800 nm output into 400 nm light via second harmonic generation (SHG). This 400 nm light is used to create a two-pass optical parametric amplifier, the output of which is a signal tunable between 470-700 nm.

Compression and Pump/Probe Generation

The output of the OPA 9400 is compressed using a pair of prisms, and this compressed output can be measured using a commercial autocorrelator (Inrad). Light of undesired visible wavelength is spatially filtered within the prism compression system.The compressed visible pulse is used to generate UV light via SHG in a β-BBO crystal (Inrad 250 μm θ=44 MgF_2 coated). The UV light and remaining visible light are separated using dichroic mirrors. The visible light is optically delayed using a computer-controlled delay stage (Klinger), then recombined with the UV and both beams are sent to the sample in a collinear geometry. For all projects described herein, the UV pulse was used as the pump, while the visible pulse was used as the probe. Figure 2.1 shows a schematic of the laser system.

2.2 Sample Containment and Cleaning

For all experiments, samples were contained under ultrahigh vacuum (UHV) conditions ($\sim 4\times10^{-10}$ Torr) to minimize surface contamination. These UHV conditions were maintained using a turbomolecular pump (Edwards EXT 255) and combination ion pump and titanium sublimation pump (Perkin Elmer TNBX). The base substrate for ionic liquid and graphene experiments was a Ag(111) single crystal (Princeton Scientific, 99.9999% purity). Ionic liquids were adsorbed directly onto the Ag(111) substrate using a commercial Knudsen effusion

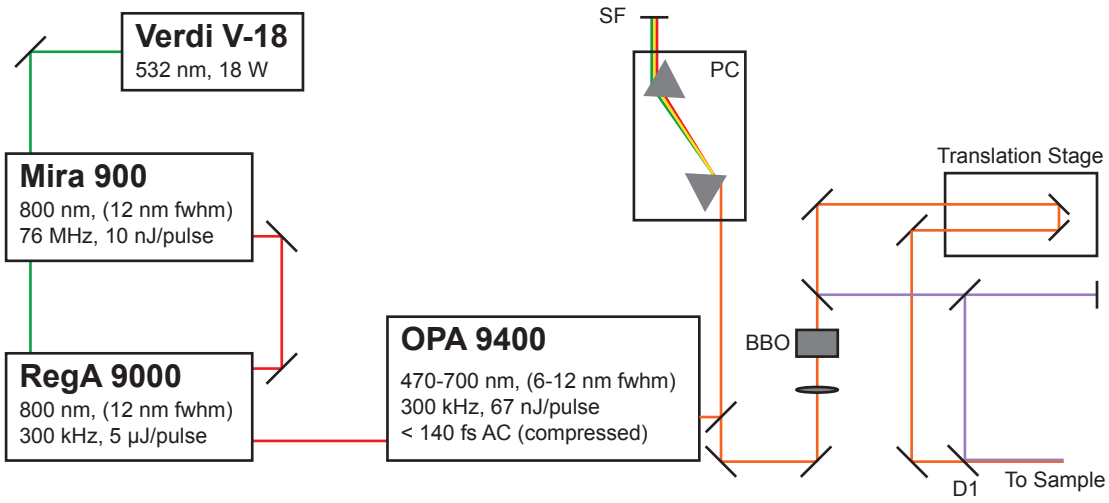

Figure 2.1: Optics are labeled as follows. PC: prism compressor using SF10 glass, SF: spatial filter used to eliminate light at unwanted visible wavelengths, BBO: β-BBO crystal cut at θ=28 and thickness 0.7 mm, D1: 700 nm long wave pass dichroic (Thorlabs). All other optics are 800 nm high-reflectors (Coherent), protected silver (Thorlabs), or UV-enhanced (Thorlabs) mirrors.

cell. Modifications made to the effusion cell setup are thoroughly described in the dissertation of Dr. Benjamin Caplins [12]. Briefly, the RTIL sample was resistively heated in a crucible to a temperature of 470 K. A aluminum shutter is oriented between the crucible and the Ag(111) substrate, this shutter could be rotated away from the crucible such that there was a clear path for molecules to evaporate onto the Ag(111) crystal.

A notable modification made specifically for RTIL epitaxy was the inclusion of a $\sim$4"$\times$4" aluminum bowl, positioned under the alumnium shutter. Ionic liquid adsorbed to the shutter would often roll down the shutter and fall off, the bowl was positioned such that the ionic liquid runoff would not fall into the turbomolecular pump positioned below the shutter. The Ag(111) crystal was cleaned by sputtering with Ar^+ ions at a pressure of $\sim 5\times10^{-5}$ Torr and sputtering current of 5-10 μA. The sputtering process was carried out for 20 minutes with the crystal held at 500 K, after which the Ag(111) was annealed at 725 K for 20 minutes. Sample cleanliness was confirmed using low energy electron diffraction (Omicron SpectaLEED) and TPPE. Gas samples could also be introduced via a precision variable leak valve. The RTIL project involved adsorbing bilayers of Xe, via introduction through the leak valve, on top of already formed RTIL films. A diagram of the side chamber used for molecular beam epitaxy is shown in Figure 2.2.

Graphene/SiC samples were prepared *ex-situ*, then mounted directly on top of an old Ag(111) crystal and held in place by stainless steel clips. This setup is shown graphically in

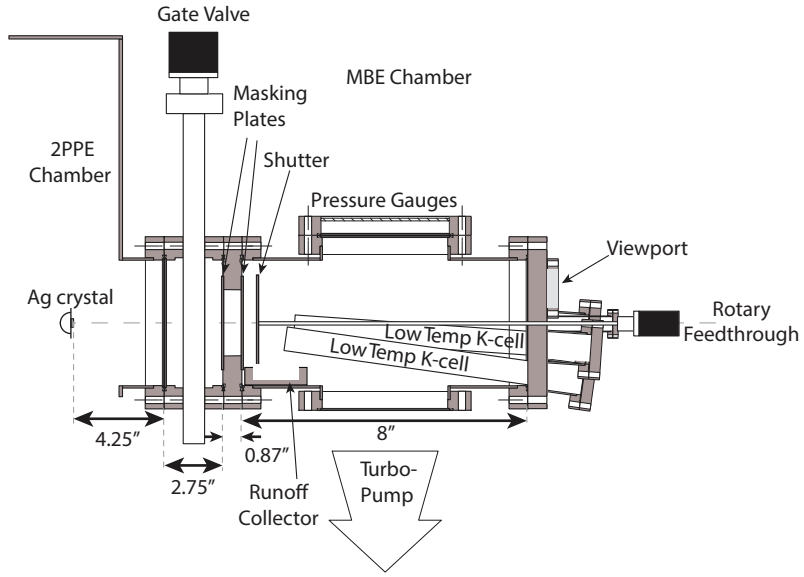

Figure 2.2: Diagram of side chamber used for molecular beam epitaxy. Two effusion cells contain samples that can be heated and cooled independently. A shutter assembly controlled by a rotary feedthrough dictates which cell has clear line-of-sight to the sample, and is therefore able to participate in dosing. A gate valve allows the entire side chamber to be isolated, and a runoff collector is positioned under the shutter assembly to catch ionic liquids that accumulate on and eventually run off of the shutter.

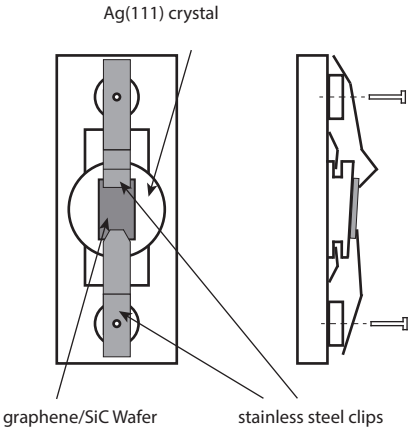

Figure 2.3: Graphene/SiC samples prepared *ex-situ* were mounted on top of an old Ag(111) crystal using stainless steel clips.

FIgure 2.3 and was designed such that Graphene/SiC samples could be mounted with minimal changes to the overall sample mounting assembly. The samples of graphene/SiC were not cleaned by the sputtering procedure described above, as the Ar^+ ions would disrupt the structure of the graphene sheets. Instead, the samples were cleaned via extended annealing $\sim$60 min at 500 K. The composition of the graphene/SiC samples was confirmed via LEED and Auger Electron Spectroscopy (AES).

2.3 Photoelectron Detection

A TPPE experiment involves introducing a pump and probe laser pulse whose combination results in the physical ejection of an electron from the sample being interrogated. This electron leaves the sample with a particular kinetic energy, which is measured here by a time-of-flight detector. The photoemitted electron travels 13.5 cm from the sample through a time-of-flight tube, and strikes a multichannel plate stack, where it is converted into an electrical pulse. The detection electronics use a start pulse given by a laser pickoff mirror and photodiode to determine the flight time of the photoemitted electron. Experimental spectra are collected by measuring $\sim 10^5$ of these single electron events, then transforming the time-domain distribution to a spectrum in the energy domain. The range of electron detection is approximately 0.3 - 5 eV with a resolution of $\sim$0.01 eV.

2.4 Temperature Programmed Desorption

Temperature programmed desorption was used to precisely calibrate the coverage of RTIL films. As discussed earlier in this work, TPD involves using a mass spectrometer to monitor a specific m/z ratio as a function of substrate temperature. As the temperature increases, molecules of different phases will be desorbed, resulting in a spectrum where each peak corresponds to a phase of the adsorbate with a different affinity for the substrate. Collecting TPD spectra as a function of different dosing conditions allowed a relationship between dosing time and sample coverage to be established. Furthermore, after every experiment involving an RTIL sample, a TPD spectrum was collected to confirm the precise coverage regime of the film under study.

A residual gas analyzer was used to perform all TPD experiments on RTIL films. An m/z ratio of 84 was used to monitor the desorption of the RTIL [Bmpyr][NTf_2]. This m/z ratio corresponds to the largest fragmentation peak of the $[Bmpyr]^+$ cation, as described by previous mass spectrometry measurements [24].

Chapter 3

Image Potential States on Graphene/SiC

3.1 Introduction

Graphene has been an intensely studied topic due to its ability to showcase unique quantum mechanical behavior and because it holds such promise for use in the next generation of high performance devices. Perhaps most notable in the context of devices is the electron mobility of this material, which can reach 15,000 $cm^2V^{-1}s^{-1}$ or more[62, 61]. This high mobility can persist with high ($> 10^{12}cm^{-2}$) concentrations of charge carriers, even in devices where physical and electrical doping is present[71]. Devices utilizing graphene's unique properties hold much promise, but the realization of this potential depends on the careful characterization of graphene in device-relevant systems.

In contrast to many reactive metal surfaces, which need to be passivated in order to be environmentally stable, graphene is naturally passivated by its π-bonding network. Graphene-based gas sensors have been developed that achieve sensitivities on the parts per billion scale and use silicon carbide (SiC) as a substrate[71, 100, 60, 64]. The SiC substrate is particularly useful because its surface not only supports the independent formation of graphene but also has a bandgap making it suitable for use in electrical devices, meaning that no transfer of the graphene is required after the sheet is formed.

Our work focuses on image potential states (IPS) because the presence and behavior of image states gives insight into the nature of the surface potential, the knowledge of which is paramount for the design of effective devices. Electrons located just outside the surface of a dielectric material experience a force attracting them to the surface; the potential in this case arises from polarization inside the material and is proportional to the inverse of z, the distance between the electron and the interface. This hydrogen-like potential gives rise to a Rydberg series of states with energies given by the expression

$$E_n = \frac{-0.85\text{eV}}{(n+a)^2} + V_0 \tag{3.1}$$

where the principal quantum number is given by n, the quantum defect parameter is given by a, and V_0 is the vacuum energy.

The formation of graphene on SiC can be achieved by a set of annealing steps which ultimately leads to graphene formation from carbon atoms of the SiC itself[42, 6]. This is in contrast with the mechanisms for graphene formation on other surfaces, where an external carbon source is needed[45, 57]. The thermal decomposition process of SiC ultimately yields sheets of freestanding graphene on the surface, but the first carbon layer formed during this process is of a different nature. The appearance of graphene-like σ bands in angle-resolved photoemission spectroscopy (ARPES) studies has shown that this $6\sqrt{3}\times 6\sqrt{3}\ R30^o$ layer, often called the "zero-layer" or "buffer layer" bears some structural similarity to graphene[25]. The buffer layer is seen to interact with the SiC substrate via strong covalent bonds between Si atoms and every third carbon atom in the buffer layer, as evidenced by energetic shifts in the ARPES spectra as well as by the results of core level photoelectron spectroscopy experiments[25]. This strong interaction with the SiC substrate is in contrast with the Van der Waals forces holding subsequently formed layers of graphene on top of the buffer layer.

Previous studies reported no IPS series on bare SiC [93], but image states were found when graphene overlayers were formed on top of SiC [88]. There is still the important issue, however, of characterizing the unoccupied electronic structure buffer layer that will be present in any epitaxially grown graphene on SiC. In the present study, we use angle- and time-resolved two-photon photoemission (TPPE) to investigate the behavior of the buffer layer and directly compare it with a 'true' graphene sample, specifically a bilayer. We find that the buffer layer supports a single image state series whose behavior is remarkably similar to that of the bilayer, despite differences in corrugation and thickness.

3.2 Experimental

Both samples are from the same n-doped 4H-SiC (0001) and were purchased from Cree, Inc. Both samples were sonicated in acetone and isopropyl alcohol and then mounted in an ultra-high vacuum (UHV) chamber. The samples were initially degassed at 550^oC for approximately 18 hours and then cooled to room temperature. The first wafer was heated to 1270^oC for 15 minutes to form 70% bilayer 30% monolayer epitaxial graphene, while the second wafer was heated to 1100^oC for 2 minutes to form the $6\sqrt{3}\times 6\sqrt{3}\ R30^o$buffer layer. The two initial samples were characterized while contained in the UHV formation chamber using low energy electron diffraction (LEED), scanning tunneling microscopy (STM), and Raman Spectroscopy. The samples were then transferred out of the first chamber, through normal atmosphere, and into a second UHV where they were kept for all subsequent experiments. The samples' exposure to air during the transfer between the two UHV chambers demanded a post-transfer characterization of identity and purity. After being transferred, both samples were annealed at 500^oC for 24 hours to remove contaminants. Auger electron spectroscopy (AES) and LEED were used to confirm that clean buffer layer and bilayer samples had been preserved [Fig 1]. The inset of Figure 4.1a shows the AES spectrum in the oxygen region,

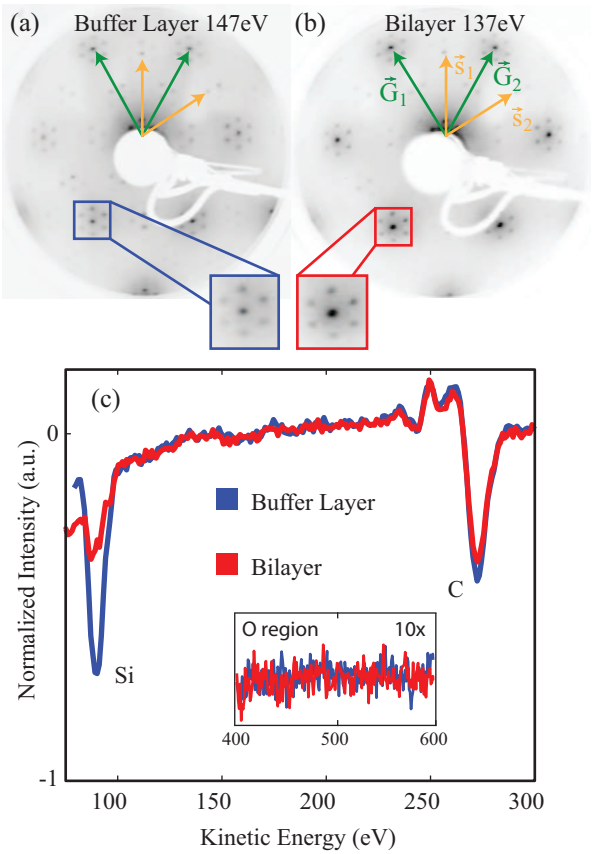

Figure 3.1: LEED images of (a) buffer layer and (b) bilayer samples. (c) Normalized and overlaid Auger spectra of buffer and bilayer samples.

the lack of peaks in this region demonstrates that the samples were free of appreciable oxidation contaminants. Qualitative inspection of the LEED data shown in Figures 1a and 1b allowed for the confirmation of our samples as buffer layer and few layer graphene. The green and gold arrows for the graphene LEED data represent vectors of the reciprocal lattices of graphene and SiC, respectively.

The set of spots defined by lattice vectors $\vec{G}_1$ and $\vec{G}_2$ exists for both the buffer layer and graphene. LEED images provide a common orientation for the two samples. Previous LEED studies have shown that the intensity of this set of spots in a graphene sample should be greater than their intensity in a buffer layer sample[70]; the insets of Figures 4.1a and 4.1b show that indeed the intensity of these spots is noticeably greater in the case of the bilayer sample. The results of AES serve to verify the lack of significant contaminants in the buffer layer and bilayer samples. Furthermore, the AES data in Figure 4.1c corroborate the identities of our samples by showing an increased ratio of C/Si peak height for the more carbon-rich bilayer sample.

The TPPE technique uses a pair of femtosecond pulses to probe initially unoccupied

states of a system. A pump pulse hits the sample at some time t_0 and serves to excite an electron from below the Fermi level (E_F) of the system into a previously unoccupied state. A second pulse is introduced at a second time t_1 to photoemit the excited state electron. Photoemitted electrons from all energetically accessible states are detected and analyzed in a time of flight (TOF) detector. Angle resolution was accomplished by rotating the sample relative to the detector, which is positioned behind a slit at an angle θ. An angle-dependent spectrum can be transformed to a dispersion relation by converting angle to electron momentum parallel to the surface $k_{\|}$ via the relationship

$$k_{\|} = \frac{\sqrt{2m_e E_{\text{photoemission}}}}{\hbar^2} \sin(\theta) \tag{3.2}$$

3.3 Results and Discussion

Details of our experimental apparatus have been previously published[49]. Figures 4.2a and 4.2b show spectra collected at non-zero pump-probe delay for both buffer layer and bilayer samples. The $n = 3$ state is not clearly visible at $t = 0$ due to its photoemission signal being overwhelmed by that of the $n = 1$ and $n = 2$. In order to show fits for all 3 IPS, spectra at two typical non-zero time delays are displayed. Figure 4.3 shows a Jablonski diagram of the buffer layer and graphene; the IPS on both samples follow a Rydberg progression typical of an IPS series. To determine which pulse was responsible for pumping the states and which served as the probe, the laser wavelength was systematically varied and shifts in the energetic positions of the peaks were observed. A linear relationship between wavelength and energetic position with a slope of 1 was found in all cases, indicating that the states are pumped by the UV pulse and probed by the visible pulse, establishing the energetic positions shown in Figure 4.3.

Angle-resolved spectra were collected for both graphene and buffer layer samples to confirm the delocalized nature of the IPS series in each case [Fig 4.2c-d]. The $n = 1$ and $n = 2$ states were fit to a Voigt peak at $t = 0$ and their dispersions were confirmed to be free-electron-like with an effective mass equal to 1.0 m_e within error, as expected for image states. The $n = 3$ peak was unable to be fit reliably as a function of angle, as its intensity was minimal at angles greater than 0. This is likely due to the state's proximity to the vacuum level; a vanishing intensity at non-zero angles suggests a dispersive state whose dispersion carries it above E_{vacuum}. It should be noted that in the analysis of these dispersion data, as well as in all other fits, all peaks are adequately represented by a single Voigt function, meaning that we do not resolve the even/odd bilayer states[8, 88]. Work functions for both samples were measured using the kinetic energies of the high and low energy cutoffs in TPPE spectra, we report a work function value of 4.26 ± 0.07 eV for the buffer layer and a value of 4.39 ± 0.07 eV for bilayer graphene (BLG), both of which are smaller than the value for highly ordered pyrolytic graphite (HOPG) of 4.49eV[87].

The π^* bands, which have often been the topic of interest in graphene[80], are not observed in our experiment due to their energetic positions, which fall well outside our

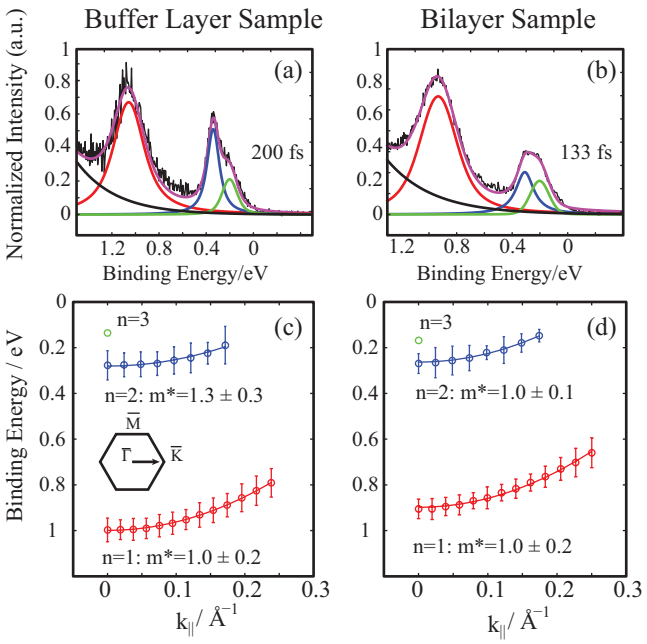

Figure 3.2: Example fits to TPPE spectra for (a) buffer layer at $t = 200$ fs and (b) bilayer at $t = 133$ fs. Red, blue and green curves represent fits for $n = 1, 2, 3$ states to Voigt lineshapes, the black curve represents a background of scattered electrons, and the magenta is the total fit. Dispersions are shown for (c) the buffer layer and (d) the bilayer; these results are taken along the direction $\overline{\Gamma} \rightarrow \overline{K}$ in k-space at $t = 0$, as shown in the inset of (c). The $n = 3$ state position is shown at $\overline{\Gamma}$, its position was unable to be reliably fit at higher $k_{\|}$ values.

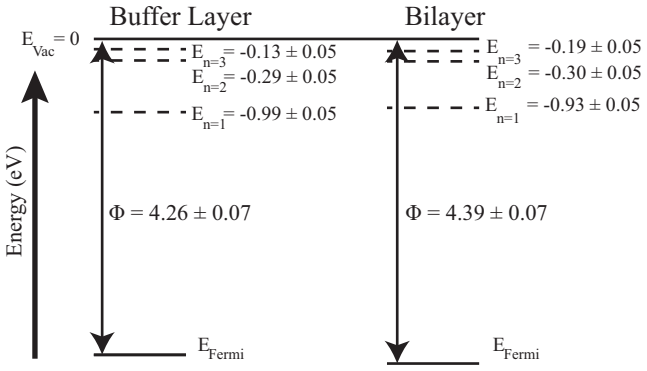

Figure 3.3: Energy level diagram illustrating the electronic states present in buffer layer and bilayer graphene at the gamma point. Work function values for each system were obtained from high and low energy cutoffs of their respective TPPE spectra.

range of detection. The π^* bands of both single layer graphene and HOPG have been shown to exist more than 10 eV above E_{Fermi} at the $\overline{\Gamma}$ and Γ points of the Brillouin zones in these materials[67, 43, 35]. Though the bands disperse downward between $\overline{\Gamma}$ and $\overline{K}$, the maximum angle of our instrument is too small for us to reach a portion of the Brillouin zone where these bands could be measured by TPPE.

In the case of all time-resolved scans, we fit the rise and decay of each IPS peak's amplitude to a single exponential function convoluted with a Gaussian instrument response function. Lifetimes of each peak were extracted from the exponential fit, and are shown alongside the data in Figure 4. For the buffer layer, the $n = 2, 3$ IPS lifetimes were 46 fs and 74 fs respectively and for the bilayer graphene sample they were 48 fs and 170 fs. Errors in lifetimes were obtained using the bootstrap method[22]. Fits were run on 1000 bootstrap data sets for each sample to obtain 95% confidence intervals for all lifetime values. The $n = 1$ state lifetimes were too short (< 30 fs) to be precisely measured with our experiment's temporal resolution. Upper and lower bounds on the $n = 1$ lifetime are drawn as a guide. A similar approach to estimate short lifetimes has been taken in photoemission experiments in the past, for example by Schoenlein et al.[72]. However, it is important to realize that these upper and lower bounds are not rigorously determined and merely serve as a qualitative guide.

One peculiarity in the case of the bilayer sample is the binding energy for the $n = 3$ state, which is unusually large given the form of Eq 1. Surface corrugation has been shown to result in large IPS binding energies[30], however, as discussed below, the bilayer sample exhibits negligible corrugation relative to the buffer layer, so this explanation can be ruled out. Large binding energies have also been explained by errors in work function measurement stemming from the presence of multiple local work functions, as highlighted in a recent study of graphene[59]. In our case, roughly 30% of the bilayer sample is actually exposed monolayer; these regions of disparate work function could lead to a similar error, giving rise to image states with large measured binding energies.

The effective masses of both $n = 1$ and $n = 2$ image states in the buffer layer are the same within error as their bilayer counterparts. This result seems obvious at first glance, since the aforementioned ARPES results indicate that the in-plane structures of buffer layer and bilayer graphene are very similar[25]. However, a 6×6 corrugation has been repeatedly observed in different coverages of graphene on SiC and it has been shown that the height modulation is greatest in the case of the buffer layer[46, 31, 69]. Image states are known to be sensitive to the effects of such corrugation; previous work on graphene/Ru(0001), for example, shows that significant corrugation of graphene can give rise to drastically different behavior when compared to a relatively non-corrugated system such as graphene/Ir(111)[58, 1]. In the case of the Ru(0001) substrate, a moiré pattern was observed to split the $n = 1$ IPS into two distinct states associated with hills and valleys of the corrugated graphene layer [1]. Earlier studies of corrugation and its effect on image state behavior show that effective masses and/or binding energies are also likely to change when an IPS is strongly affected by corrugation[30]. We observe a slight effective mass increase of the buffer layer $n = 2$ state relative to its bilayer counterpart and a binding energy increase for the buffer layer's $n = 1$

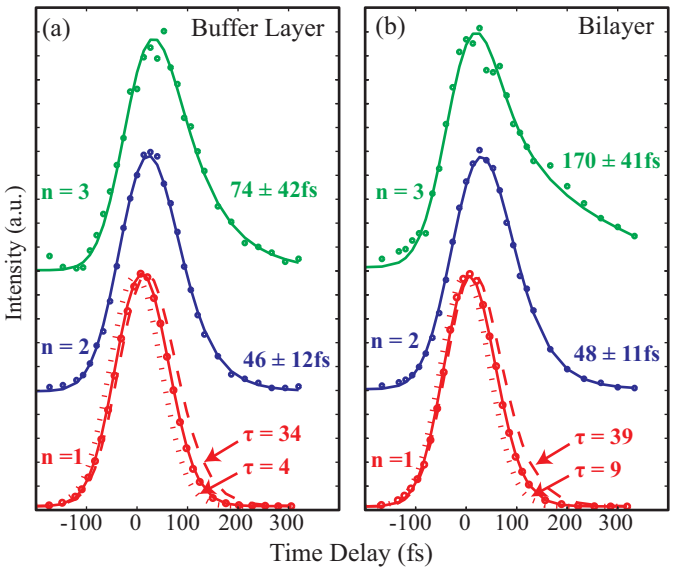

Figure 3.4: Time-resolved measurements at $\overline{\Gamma}$ for (a) buffer layer and (b) bilayer samples. Error bars reflect 95% confidence intervals obtained using the bootstrap method[22]. Dotted and dashed lines are fits with time constants fixed at the displayed values, they represent qualitative lower and upper bounds for the $n = 1$ states, respectively.

state, but the binding energy of the $n = 3$ state of the buffer layer is actually smaller than that of the bilayer and the $n = 2$ binding energies are almost identical, as are the values of effective mass for the $n = 1$ states.

To reiterate, we would expect an IPS series strongly affected by corrugation to have a significantly different set of binding energies and/or m^* values when compared to its non-corrugated analog, and a strongly interacting situation would be expected to lead to a split of the $n = 1$ state. The lack of a definitive and consistent set of differences in m^* or binding energy between the buffer layer and bilayer samples, as well as the absence of a split of the $n = 1$ state of the buffer layer, indicates that the image states in the buffer layer sample are not significantly perturbed by surface corrugation; they behave the same as their bilayer counterparts in these respects. Any future work studying, for example, adsorbed species atop graphene/SiC can safely say that any significant alteration of image state energetics or dispersion in their system comes directly from the adsorbed species itself. This result is meaningful given the continuing interest in these types of studies and the particular importance of the SiC substrate to graphene-based devices.

Our measurements show an increase in lifetime with principal quantum number n for both the buffer layer and bilayer samples. The lifetimes of the bilayer's $n = 2$ and $n = 3$ states are longer than those of the buffer layer, indicating that wavefunction overlap with the substrate plays a role the decay pathway, as has been known for image states. The lifetimes we observe in the bilayer, however, are actually shorter than those reported for monolayer graphene on a variety of metal substrates [59]. As pointed out by Takahashi et. al., the

lifetime of image states on the SiC substrate may decrease because they will be resonant with bulk bands, which is not the case for metal substrates such as Ni(111) or Ir(111) that were previously studied [59]. Nevertheless, graphene's large band gap at $\overline{\Gamma}$ should allow it to serve as a dielectric screening layer[78]. If the decay pathway for the IPS were a simple coupling to the SiC conduction band, one would expect the lifetimes of all states measured at $\overline{\Gamma}$ to increase exponentially as the thickness of the graphene layer was increased. In fact, there is very little difference in $n = 2$ lifetimes: the only noticeable difference is in the $n = 3$ states, where the bilayer $n = 3$ lives a little over twice as long as that of the buffer. It seems likely, then, that the graphene layers themselves play a role in the decay of IPS electrons, with the effect being more pronounced for the $n = 3$ state whose wavefunction is concentrated farther from the SiC substrate.

3.4 Conclusion

From the results of dispersion and time-resolved measurements, as well as from energetic peak spacing, it is clear that the states observed on the buffer layer belong to an IPS series. The same set of measurements on a bilayer graphene sample yield another IPS series with exceedingly similar behavior, the main difference being an extended $n = 3$ state lifetime. The effects of structural differences stemming from the reconstructed and corrugated nature of the buffer layer were found to be negligible. This study has shown that, while the buffer layer of graphene on SiC is often regarded as unlike subsequent graphene layers, an image state series exists even when only this buffer layer is present. It is well established that the buffer layer lacks many of the unique properties of free standing graphene due to its π system being disrupted by covalent interactions with the substrate. However, by characterizing the IPS series of the buffer layer and demonstrating its similarity to that of bilayer graphene, we have shown that the buffer layer gives rise to a surface potential which appears equivalent to that of free standing graphene. This is significant given the role of the surface potential in graphene-based sensors and other modern devices.

Chapter 4

Impact of Film Thickness and Temperature on Ultrafast Excess Charge Dynamics in Ionic Liquid Films

4.1 Introduction

Room temperature ionic liquids (RTILs) have been a focus of research in recent years due to their unique set of properties such as high electrochemical stability and ionic conductivity, very low vapor pressure, and easily tunable structure[15, 14]. These characteristics have made RTILs useful in a variety of applications ranging from green solvents for synthesis and catalysis[33, 101, 99, 21] to lubrication and processing of spent nuclear fuel[102, 94, 86]. RTILs have also been explored for use in electrochemical devices such as Li^+ batteries[38, 48] and electrical double layer capacitors[28, 68, 10] (EDLCs). Electrochemical reactions that determine the performance of devices such as EDLCs happen at or near the RTIL/electrode interface, and understanding interfacial RTIL structure and dynamics is important to further develop these devices [4, 51, 27, 92, 5, 20, 50, 19, 11].

Herein we expand this existing knowledge of interfacial RTIL behavior by focusing on ultrafast dynamics of RTIL films. Specifically, the goal is to investigate ultrafast excess charge solvation in thin films of ionic liquids on a metal electrode. Solvation of charged species has been studied extensively in both traditional solvents [18, 13, 40, 23, 44, 73, 77, 90, 98] as well as in bulk RTILs[16, 37, 2, 3, 39].It has been shown that solvation in bulk RTIL systems is often multiexponential and the timescale of the process can span multiple orders of magnitude with components as short as ¡ 100 fs[15, 16, 2, 29]. Subpicosecond dynamics are often attributed to librational motion, while dynamics on longer timescales are assigned to diffusion of solvent molecules [16, 36] Until recently, however, there was no study of charge solvation in an RTIL which investigated interfacial dynamics on the 100 fs timescale[55].

Such a study is important to carry out, as it has been shown that changes in dimensionality of surface systems can lead to new, interesting behavior that is distinct from the bulk[52].

Previously, we investigated the solvation response of a film of the ionic liquid 1-butyl-1-methylpyrrolidinium bis(trifluoromethylsulfonyl)- imide ([Bmpyr][NTf_2]) on the sub- picosecond timescale[55]. While this study was an important first step toward establishing an understanding of RTIL behavior at surfaces, the structure of the film itself was not a focal point of the study because the molecular geometry was not well understood at the time and an appropriate technique for precisely determining film coverage was not available in our laboratory. More recently, microscopy measurements, as well as DFT-based simulations, have shown how [Bmpyr][NTf_2] adsorbs on the Ag(111) surface at a molecular level[11]. The present study builds upon our group's previous results by linking solvation behavior in the same [Bmpyr][NTf_2]/Ag(111) system to well-defined film coverages and the newly described liquid-like and crystalline phases[11], as well as investigating the spatial location and origin of states observed at the interface. We use temperature programmed desorption (TPD) in conjunction with two-photon photoemission (TPPE) spectroscopy to study excess electron dynamics in films of well-known coverages in two different temperature regimes. We show that RTIL films can indeed be grown that support multiexponential solvation processes that are similar to those observed in bulk RTIL materials. Furthermore, we discuss the origin and spatial location of the interrogated interfacial states, the role of screening in the RTIL films, and the effect of film phase on the observed dynamics. The results of this study lay the groundwork upon which more complex structural and dynamical investigations will be based, and are therefore a critical step toward realizing the full potential of RTILs.

4.2 Experimental

All experiments were performed in an ultra-high vacuum (UHV) chamber with a base pressure of $< 5 \times 10^{-10}$ Torr. The samples could be either resistively heated or cooled using a liquid nitrogen/helium cryostat, allowing the sample to reach temperatures as low as 60 K and as high as 700 K. A Ag(111) single crystal (Princeton scientific, 99.999%) was used as the substrate for all films. The Ag (111) sample was cleaned by standard Ar^+ sputtering and annealling, and cleanliness was confirmed by the observation of Ag surface states in TPPE spectra. A sample of 1-butyl-1-methylpyrrolidinium bis(trifluoromethylsulfonyl)imide (IOLITEC, 99.5%) was loaded into the UHV chamber and repeatedly degassed between 450-470 K over the course of several days. Deposition of the RTIL was performed using a commercial effusion cell setup. The dosing rate was carefully calibrated using both TPPE and temperature programmed desorption (TPD). Both of these techniques independently showed that heating the RTIL at 470 K while holding the Ag (111) electrode at 300 K resulted in a dosing rate of 0.1 ML/min (see Supplemental Information).

A commercial Ti:Sapphire oscillator and 297 KHz regenerative amplifier were used to perform all TPPE experiments, the setup we used for this study has been described in detail elsewhere [49]. Briefly, the Ti:Sapphire system was used to pump an optical parametric

amplifier (OPA). The visible output of the OPA and its second harmonic were used as probe and pump pulses, respectively. The cross correlation between pump and probe was measured to be 120 fs, while the laser bandwidth was approximately 25 meV. The work functions of all films were measured by the onset of 1PPE, these measurements allowed us to determine binding energies relative to the vacuum level.

As will be discussed in more detail later, the RTIL films were found to degrade under prolonged laser exposure. Since the goal of our study is to investigate solvation response in an unperturbed film, extensive experiments were done to establish a maximum allowable exposure time that could be used for all collected data. The intensity change per second was calculated at a series of different time delays for each coverage, and it was determined that in the absolute worst case scenario of a thick 3 ML film at a 200 ps delay the intensity change would be under 10% for a 15 second integration time. Collection times of 15 s were therefore used for all scans, and after each collection the laser position on the crystal was moved to provide a sample of fresh film (see Appendix B).

4.3 Results and Discussion

Initial Characterization of Ultrafast Response

Angle-resolved two photon photoemission spectroscopy (TPPE) was used to characterize the dynamic behavior and degree of localization among electronic states in films of [Bmpyr][NTf_2]. In the first step of TPPE, a pump pulse excites an electron from below the Fermi level of the metal substrate into an intermediate state below the vacuum level of the system. Dynamic processes, such as electron transfer between interfacial states or solvation response, take place, after which a probe pulse is used to photoemit the electron from the intermediate state. The photoemitted electron is collected by a time-of-flight (TOF) detector, where its energy is analyzed. The details of TPPE are well described in a previously published review [65].

Figure 4.1 shows a typical time-resolved TPPE experiment in a [Bmpyr][NTf_2] film. A 2 ML film at 300 K is shown in Figure 4.1(a), where what appears to be a single, broad feature is bound to the vacuum level at t=0 by approximately 0.5 eV. This peak gains binding energy rapidly for the first picosecond, then continues to relax more slowly over another few picoseconds. At a lower temperature of 130 K, a single peak is again observed with a binding energy of c.a. 0.5 eV at t=0, as shown in Figure 4.1(b). However, at 130 K relaxation only occurs in the first 500 fs with the peak shifting by only c.a. 0.3 eV. After 500 fs, the feature again persists for a few picoseconds, but without additional relaxation. The main goal of this study will be to describe what state or states are being observed in this type of time-resolved measurement and what processes might be responsible for the ultrafast dynamics that we observe, and for the dramatic difference between films under different conditions.

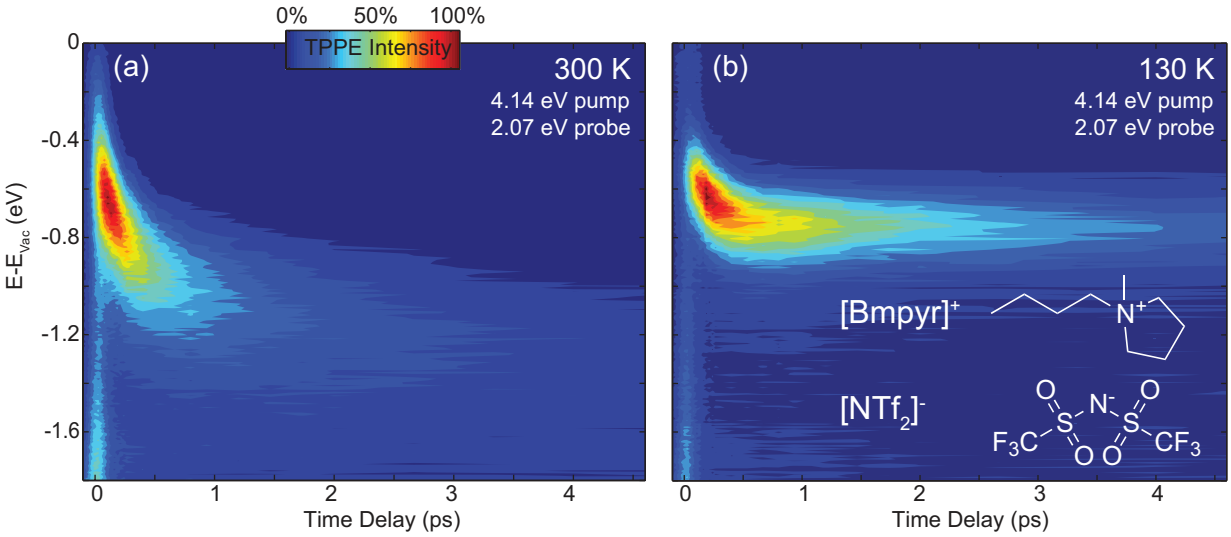

Figure 4.1: False color contour plot of a 2 ML [Bmpyr][NTf_2] film on Ag(111) at (a) T = 300 K and (b) T = 130 K .

Surface States and Localization

We use angle-resolved TPPE measurements to investigate localization of the states at the film/vacuum interface and elucidate their physical origin. The parallel momentum of an interfacial electron is given by $k_{||} = \sqrt{2m_e E_{kin}/\hbar^2} sin(\theta)$, where m_e is the electron's mass and E_{kin} is the measured kinetic energy. Angle-resolved TPPE can be used to map out interfacial band structure by varying the angle θ between the sample and the detector. Fitting the experimental dispersion relation to the expression $E = E_0 + \hbar^2 k_{||}^2/2m^*$ yields the effective mass, which reflects the localization of the electron. An effective mass with an absolute value of approximately one or smaller is indicative of a highly delocalized state, while an effective mass with an absolute value much greater than one signifies a localized state.

Initially treating the broad RTIL feature as a single state resulted a single dispersion curve whose effective mass slowly transitioned from positive to negative. A similar, continuously changing dispersion was described previously by Wolf et. al. for their initial treatment of TPPE data from the D_2O/Cu(111) interface. In those studies, further and more detailed fitting led to the conclusion that two distinct states were present in D_2O/Cu(111) at early times[9]. The approach in our present study was similar, and the same conclusion is reached here: two distinct interfacial states are present at the [Bmpyr][NTf_2]/Ag(111) interface.

Figure 4.2 shows the results from angle-dependent measurements on a 0.9 ML film at 130 K. A submonolayer coverage was used so that no complications would arise from the presence of small patches of overlayers. Two peaks are required to adequately fit the RTIL feature at time delays less than 200 fs, particularly at high angle. The two peaks labeled states A and B represent two distinct states that exist simultaneously for the first 200 fs

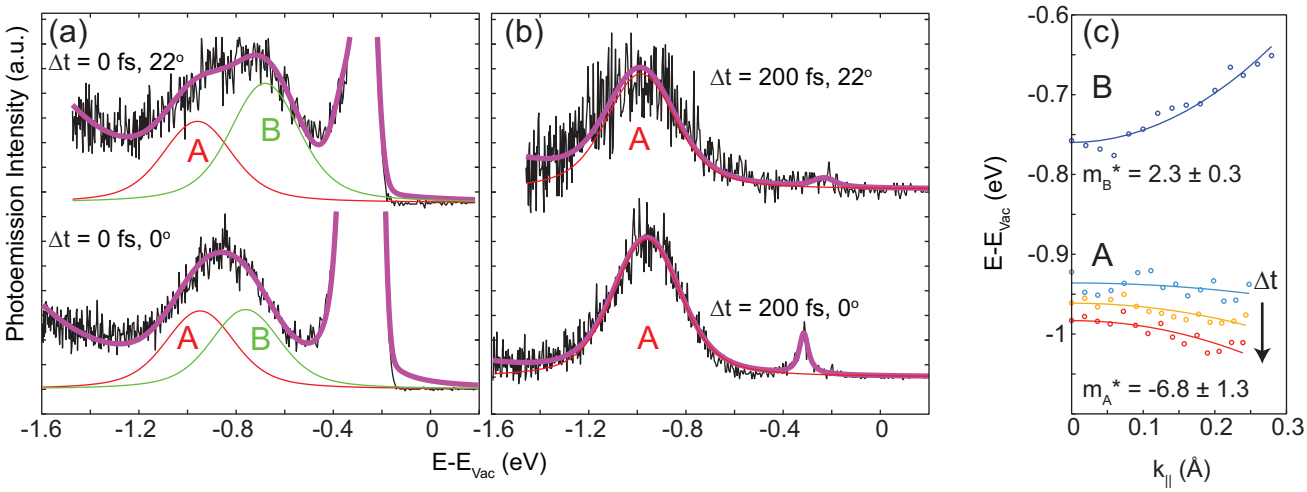

Figure 4.2: Panel (a) shows angle-resolved spectra which resolve two states in a 0.9 ML film at 130 K. The same angle slices are shown in (b) after 200 fs: only a single state remains. Dispersion relations for states A and B are presented in (c). The weakly bound state B shows a positive dispersion indicating delocalization, while the more strongly bound state A has a large valued and apparently negative effective mass, indicating a localized state. The dispersion curves for state A become more strongly bound over time, they represent slices at t_{delay} = 47 fs, 200 fs, and 267 fs.

after charge injection into the film. Figure 4.2c shows the dispersion relation for the two peaks. The precursor state B has a positive dispersion relation with a small effective mass of 2.3 ± 0.3, indicating a delocalized state, while state A has an apparently negative dispersion relation averaging to -6.8 ± 1.3. The large feature around 0.3 eV comes from surface states of the bare Ag(111), some of which are still visible due to the submonolayer coverage regime.

Given the sub monolayer coverage and positive effective mass, we assign state B to an IPS perturbed by the presence of the RTIL film. The large absolute value of state A's effective mass as well as its strong solvation shift provide evidence that state A is localized. As mentioned above, our energetically broad, localized, and solvated state is very similar to the one found on D_2O/Cu(111) [9]. When shorter laser pulsewidths are used, the electron transfer from the precursor to the solvated state can in principle be accessed, as has been recently demonstrated for electrons injected into ice on Cu(111) [81]. However, the 120 fs correlation precludes such an analysis in the present work and we focus on the longer timescale solvation dynamics.

Solvation: Binding Energy Shift

The results shown in Figure 4.1 demonstrate that film conditions, specifically film temperature, can qualitatively alter the nature of the response to excess charge. We now take a systematic and more quantitative approach to outline how film conditions, specifically both

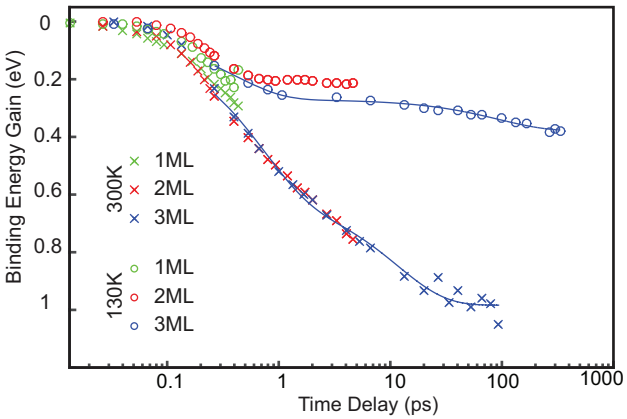

Figure 4.3: The increase in binding energy of the solvated state as a function of time delay is shown for films of different thickness at 300 K and 130 K. Solid lines represent biexponential fits to 3 ML data between 250 fs and the maximum time delay for a given collection.

film thickness and temperature, have an impact on the solvation process.

Shown in Figure 4.3 is the binding energy gain of the RTIL feautre, E(t)-E(t_0), as a function of time delay for films of thickness 1-3 ML and temperatures 300 K and 130 K. These results were obtained by fitting to a single Voigt peak, though we showed in the previous section that two distinct states can be resolved at short (¡ 200 fs) times in a 1 ML film. Increased broadening seen in thicker films led to an inability to resolve two distinct states at early time delays, we therefore make the approximation of using a single Voigt lineshape in order to have a consistent metric by which to compare results among films of different coverage. We point out that although this approximation is not ideal, it will only introduce error within the first 200 fs. Furthermore, the error in binding energy expected from fitting to a single peak at different coverages should be consistent across different coverages, allowing the results from different films to be compared.

The trajectory for all coverage and temperature combinations is equivalent up until approximately 500 fs, implying that the initial relaxation steps are independent of coverage and temperature. It seems likely that the localization process is dominating the dynamical energy shift on this timescale, and that this localization is equivalent across differently prepared films. After c.a. 500 fs, the data is split between 300 K films which continue to relax rapidly and 130 K films whose relaxation rate slows down. To better compare solvation in the two temperature regimes, we quantified our description of solvation in 3 ML films by fitting the time-dependent binding energy shift to a biexponential function, similar to what has been done in bulk RTIL solvation studies[2]. The results of this analysis are shown in Table 4.1, the time window for the fits began at 250 fs in order to avoid complications from the precursor state B. The faster time constant in both 300 K and 130 K films is similar; both are on the order of a few hundred femtoseconds. The main difference is in the longer time constant, which is nearly an order of magnitude greater in the 130 K films versus films at 300 K. From these results, it can be seen that the initial relaxation steps occurring on the

Table 4.1: Biexponential Fit Parameters for Solvation Shift in 3 ML Films

T (K)	A_1 (eV)	τ_1 (ps)	A_2 (eV)	τ_2 (ps)
300	0.52 ± 0.04	0.48 ± 0.07	0.48 ± 0.02	7 ± 1
130	0.24 ± 0.05	0.32 ± 0.06	0.10 ± 0.01	64 ± 15

100's of femtoseconds timescale are indeed similar for both temperature regimes, but that the solvation process is dramatically different on the picosecond timescale.

The differences in solvation behavior between 130 K and 300 K films likely come from dissimilarity in the physical structure of films in these temperature regimes. As shown in previous work[11, 55], the [Bmpyr][NTf_2]/Ag (111) system undergoes a phase change between 130 K and 300K, the two temperatures used in the present study. Recent STM results show that films at 130 K will be dominated by a crystalline structure while films at 300 K will be primarily diffusive and liquid-like[11].

As shown in Figure 4.3 and Table 4.1, the energetic relaxation of excess charge continues rapidly for the duration of the experiment in liquid-like films at 300 K, leading to a total solvation of almost 1 eV in 3 ML films and a longer time constant of 7 ps. Meanwhile, the binding energy in crystalline films at 130 K relaxes more gradually, resulting in a longer time constant of 64 ps, and the total solvation even after hundreds of picoseconds is less than 400 meV. A likely explanation for this difference in behavior is that the diffusive molecules of the liquid-like films at 300 K are able to move more freely, allowing for a stronger response to the injected excess electron and resulting in larger solvation energy. This assignment is supported by previous studies of solvation in bulk ionic liquids, which link slow nonexponential dynamics to the phase-sensitive process of ionic diffusion[74].

Population Dynamics and Solvation Location

Time-resolved population dynamics of the solvated state are obtained by fitting the peak in each TPPE spectrum at a series of time delays to a single Voigt lineshape, then tracking the amplitude of that peak as a function of time. The fits to these data start at 250 fs and continue until the S/N was less than approximately 2/1. This temporal window was chosen such that the solvation process could be fit simply and reproducibly without interference from the delocalized precursor state (state B) described above. Figures 4.4a and 4.4b show the normalized time-dependent amplitude as a function of time for films of thickness 1-3 ML and temperatures of 300 K and 130 K. Solid lines represent fits to one, two, and three exponential functions for coverages 1-3 ML, respectively.

Table C.1 reports average lifetimes computed by weighting the time constants used to fit the population data at a given coverage by the equation $\tau_{avg} = \sum_{i=1}^{N} a_i \tau_i^2 / \sum_{j=1}^{N} a_j \tau_j$ (See Appendix C). These results show that the average lifetime of the excess electron increases by as much as 5 orders of magnitude as film thickness increases from 1 to 3 ML. The

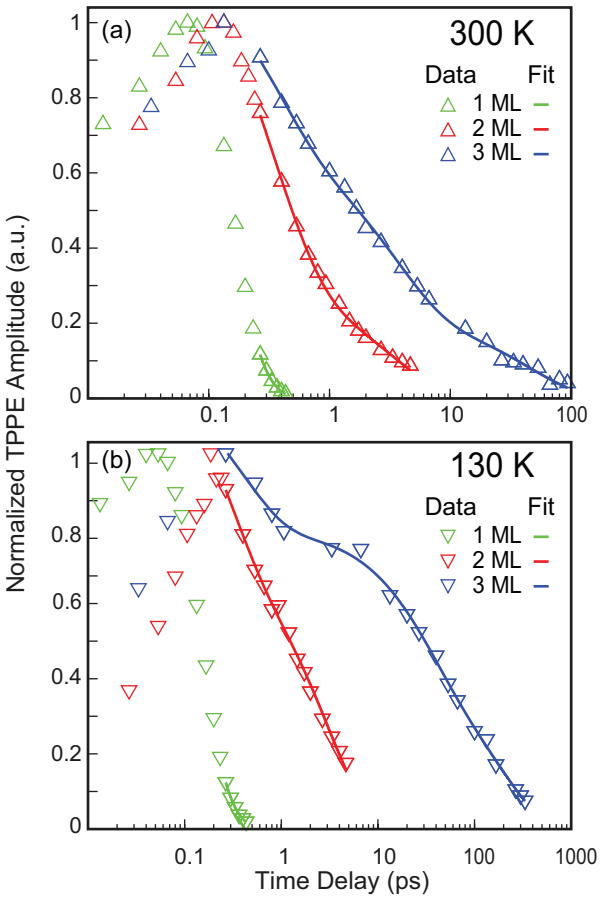

Figure 4.4: Population dynamics of multiple coverages at 300 K and 130 K are fit to exponential functions; fit results are presented in Table 1. The data are fit from 250 fs onward such that they describe population dynamics of the solvated state only, without interference from the short-lived delocalized state B.

reorientation of molecular dipoles within the RTIL film during the solvation process would result in the emergence of a tunneling barrier that will affect the state's lifetime, as has been described previously [82]. However, the solvation shifts for RTIL films of different coverages are equivalent within our experimental uncertainty (see Figure 4.3), which implies that the nature of the solvation response itself is also equivalent for the thickness regimes investigated here. These trends lead us to conclude that as film thickness increases, the distance between the confined, solvated state and metal substrate increases and this results in a decreased wavefunction overlap between solvated state and metal substrate. This situation creates a tunneling barrier whose width increases with film thickness resulting in an increased lifetime. This conclusion implies that solvation is not occurring directly at the interface between the Ag (111) electrode and the RTIL film, but it is difficult to conclude more about solvation location based on these data alone.

Table 4.2: Average time constants for coverages 1-3 ML at 300 K and 130 K

T (K)	Coverage (ML)	Avg Lifetime (ps)
300	1	0.07 ± 0.02
	2	2.5 ± 1
	3	62 ± 46
130	1	0.09 ± 0.02
	2	3.0 ± 0.5
	3	195 ± 83

To further elucidate the location of electron solvation, we collected TPPE spectra after adsorbing 2 ML Xe onto a 2 ML film of [Bmpyr][NTf_2]. Charges solvated in the bulk of a film such as [Bmpyr][NTf_2] are expected to be screened by surrounding solvent molecules, preventing interaction with the adsorbed Xe and leading to TPPE spectra that are similar to those taken in the absence of Xe overlayers. Titration of D_2O ice multilayers with Xe, for example, showed negligible binding energy shift of the observed solvated state, indicating that the state is situated inside the multilayer ice film[85]. Solvation occurring at the film/vacuum interface, on the other hand, is expected to lead to the solvated charge being significantly affected by the presence of polarizable and confining Xe atoms[83]. In the case of solvation at the surface of other thin film solvent systems such as NH_3 on Cu(111) and clustered D_2O on Cu(111), TPPE spectra collected in the presence of Xe adlayers resulted in a significant (∼300-400 meV) shift in the binding energy of the solvated state as well as suppression of that state's intensity[83, 84].

As shown in Figure 4.5, titration of 2 ML [Bmpyr][NTf_2] with 2 ML Xe resulted in a relatively small energetic shift relative to the shifts seen previously in other thin film surface-solvating systems, which were on the order of several hundred meV. The change in work function upon Xe adsorption was taken into account in these spectra, and the small magnitude of this shift observed for [Bmpyr][NTf_2] films might suggest that solvation proceeds within the film itself, similar to the case of multilayer D_2O. However, Figure 4.5 also shows the significant decrease in photoemission intensity in a Xe-titrated film relative to the neat IL counterpart. We would expect that a state completely buried within the RTIL film would show neither an energetic shift nor a substantial change in photoemission intensity upon adsorption of a dielectric overlayer, as was the case with the solvated state of D_2O multilayers [85] and the higher (n ¿1) IPS in NaCl [56]. Though the magnitude of the energetic shift observed in the RTIL is small, we assert that our observation of a non-zero energetic shift along with the significant intensity decrease of the state is evidence that solvation occurs primarily near the RTIL/vacuum interface. The significant change in solvated state lifetime with increasing coverage (see Table 2) provides additional evidence that we are observing a solvation process oriented at the surface of the RTIL film.

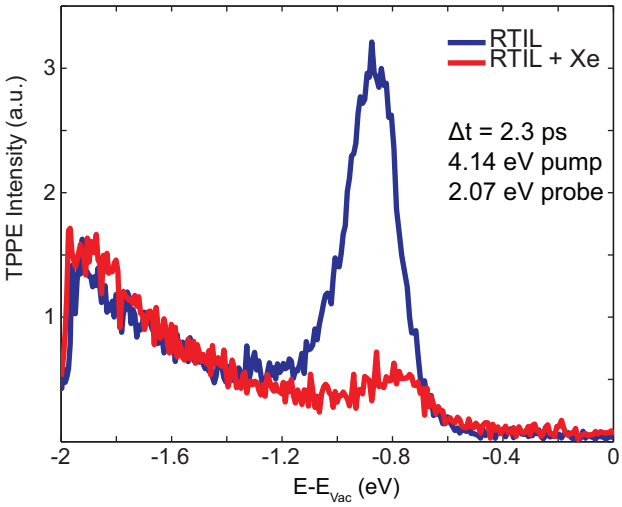

Figure 4.5: Overlaid TPPE spectra for 2 ML RTIL and 2 ML RTIL + 2 ML Xe are shown. Only a small change in the BE of the solvating state is observed after growth of 2 ML xenon, but the large decrease in photoemission intensity points to a significant interaction between state A and molecules in the Xe overlayer and implies that solvation occurs at the surface of the RTIL.

Relaxation Mechanism and Degradation

With the trends linking solvation response to RTIL coverage and temperature now established, the physical origins of the two states B and A can be addressed. The localization characteristics and timescales we observe with TPPE are qualitatively similar to the results of a recent theoretical study by Margulis et. al. In that study, it was shown that an initially delocalized 'dry' excess electron in bulk [Bmpyr][NTf_2] becomes localized on an [NTf_2]$^-$ anion after 40 fs, resulting in a fragmentation of the RTIL molecule over the course of a few picoseconds [97]. Though our precursor state B would be fundamentally different from the 'dry' state due to the presence of the metal electrode, we nevertheless observe a situation that is similar to the one predicted by Margulis: a delocalized initial state which transfers population into a localized state on a sub-100 fs timescale. Furthermore, we find strong evidence for film photodegradation, suggesting that we may be observing a dissociative electron attachment mechanism in our [Bmpyr][NTf_2] films.

Photodegradation can be observed indirectly using TPPE by examining the effect that prolonged laser beam exposure has on the intensity of the RTIL feature at a series of time delays. The data from a 'before-and-after' experiment, presented in Figure 4.6, were taken at the same laser power and are presented on the same color scale, making them directly comparable. These data show that laser exposure over a period of 30 minutes has a dramatic impact on the film behavior, as reflected in the marked intensity loss for time delays $\geq$ 200 fs. If the current TPPE experiments are observing anionic attachment followed by fragmentation

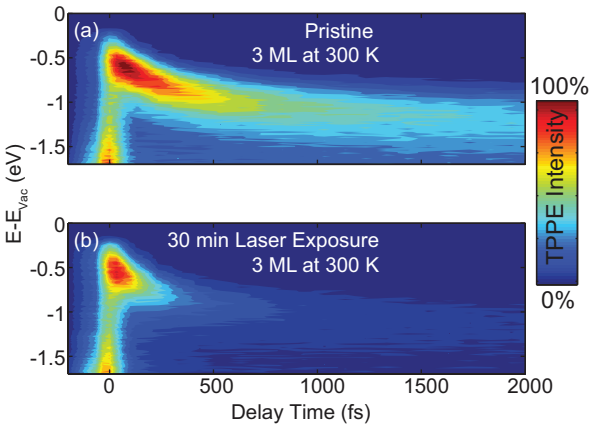

Figure 4.6: Prolonged laser exposure results in film degradation. Panel (a) shows the dynamic scan of a 3 ML film at 300K. Panel (b) shows the same film after 30 minutes of laser exposure. The film in (b) is at the same temperature, the same laser power was used, and the result is plotted with the same color scale.

and solvation of a fragment, as suggested by previous work, then prolonged laser exposure would result in a depletion of pristine $[NTf_2]^-$molecules. The excess electron could be injected into the initial delocalized state, but would then have no unfragmented anions to attach to and the ps timescale solvation process would never occur. The experimental result of this set of processes would be what is observed here: relative to a non-exposed sample, TPPE intensity around delay time zero would be mostly preserved while intensity in the picosecond range would be significantly decreased.

Degradation of ionic liquids has attracted much attention in the literature over the last 15 years, and several studies have elucidated specific degradation pathways often using techniques involving either radiolysis[75, 76, 32, 7, 47] or photodetachment[53, 41, 26, 17, 89]. A few possibilities that exist are that the $[NTf_2]^-$ anions on the Ag(111) surface photodegrade by a breaking of the N-S bond, a C-F bond cleavage may be involved, or it is possible that some combination of these two options or others is taking place. Though we do not claim that our results support a specific degradative mechanism, it is important to show that a photoinduced change is taking place in our films which is likely related to degradation of one or both constituent ions. Our qualitative picture of degradation is an interesting potential link between surface and bulk behavior of RTILs, as well as being useful to future spectroscopic studies of RTIL films.

4.4 Conclusion

The ultrafast solvation behavior of the RTIL [Bmpyr][NTf_2] at three coverages and in two temperature regimes has been characterized using time- and angle-resolved TPPE. Angle-resolved measurements revealed the presence of two states, one of which was delocalized

and became depopulated after c.a. 200 fs and the other of which was localized and had a lifetime between 0.07 ps and 195 ps depending on film conditions. It was found that the events following electron injection are similar in nature for all films, differences among films of dissimilar temperature were evident at later (< 500 fs) delay times. It was determined that film thickness did not change the nature of the solvation process itself, the most significant effect of changing film thickness was a dramatic change in solvated state lifetime. Xenon overlayer experiments suggested that the solvation process occurs near or at the film/vacuum interface. Degradation was observed and qualitatively described; similarity to results in the literature suggests that the solvation process may involve radical species. This has been the first study of its kind that links dramatic changes in ultrafast behavior of an interfacial RTIL system to structural characteristics such as film thickness. These results are an exciting first step toward a more complete understanding of interfacial RTIL behavior, and will likely serve as a key foundation upon which further interfacial studies can be built.

Chapter 5

Characterization of Non-Degrading Ionic Liquid Interfaces

5.1 Introduction

A great strength of RTIL's, one that makes them attractive for use in a variety of industries, is the ability to tune the properties of an ionic liquid system by changing the identity of cation and/or anion. The vast number of cation/anion combinations that are available make it likely that there exists an ionic liquid that matches most requirements. The previous chapter describes how TPPE was shown to be a powerful technique for investigating the behavior of electronic states in an interfacial sample of a single RTIL: [Bmpyr][NTf_2]. Ideally, however, a variety of RTIL materials would be surveyed, so that trends in interfacial behavior could be established. This chapter describes preliminary TPD and TPPE results from experiments on a second RTIL species: 1-butyl-1-methylpyrrolidinium dicyanamide ([Bmpyr][DCA]).

5.2 Sample Formation

As was done in the case of [Bmpyr][NTf_2], dosing conditions of the RTIL [Bmpyr][DCA] were carefully calibrated using a combination of dose-dependent TPD and TPPE measurements. Figure 5.1(a) and (b) show results from TPD and TPPE experiments, respectively. The [Bmpyr][DCA] samples were dosed from a ceramic crucible that was held at 430 K for the duration of the sample formation process. During dosing, the Ag(111) substrate was held at 128 K. The TPD spectra in Figure 5.1(a) show a monolayer peak at around 270 K, and a multilayer peak at approximately 180 K. Qualitatively examining these TPD spectra gives much information about how this RTIL grows. For example, the monolayer peak is nearly saturated after 20 minutes of dosing. This dosing rate is roughly 1/2 of the rate at which [Bmpyr][NTf_2] was dosed (see Appendix A). Qualitatively, the TPD spectra of [Bmpyr][DCA] is very similar to that of [Bmpyr][NTf_2], suggesting that the two RTIL's grow similarly during the dosing process.

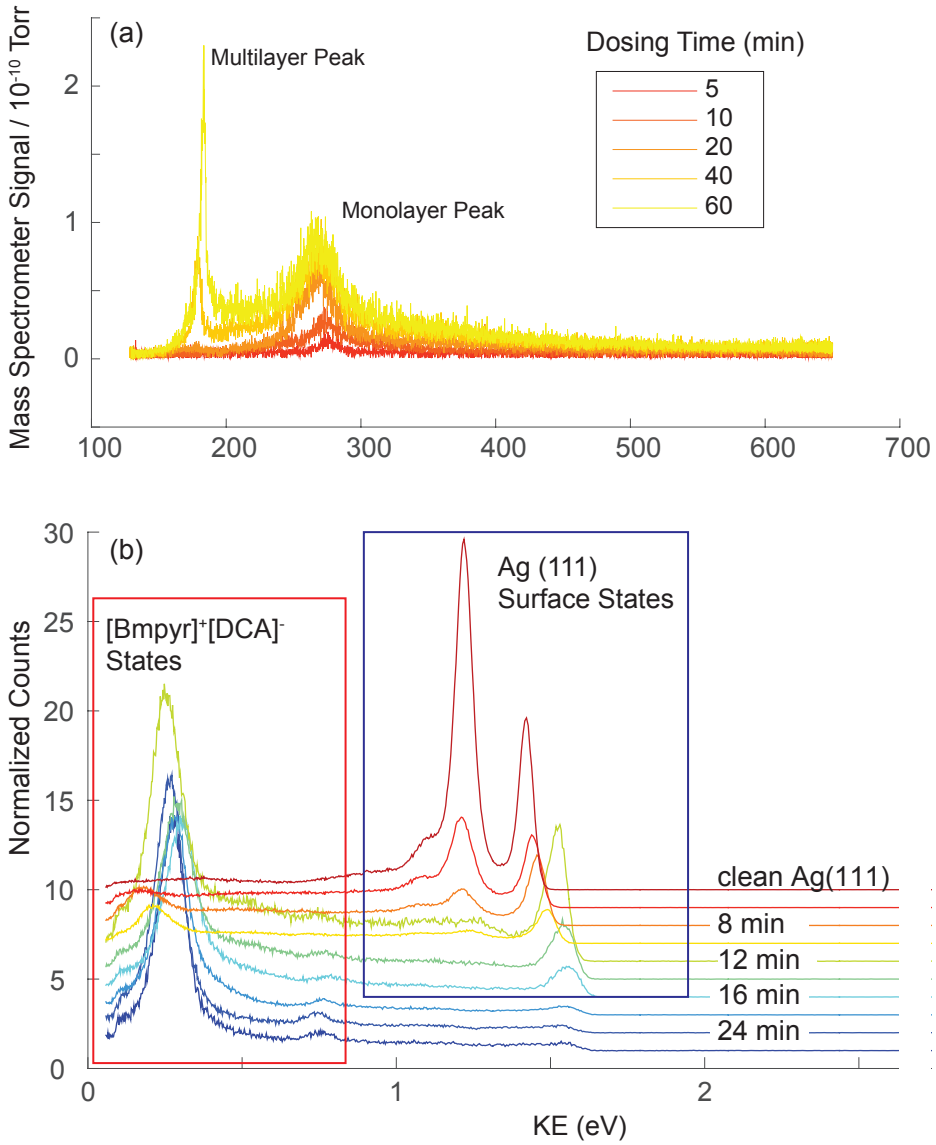

Figure 5.1: Sample formation is characterized using TPD and TPPE measurements, shown in (a) and (b) respectively. Dosing was performed from a crucible held at 430 K, while the Ag(111) substrate was held at 128 K. The TPD spectra in (a) show a monolayer peak at ∼270 K and a multilayer peak at ∼180 K. The TPPE spectra in (b) show gradual quenching of Ag(111) surface states accompanied by growing in of [Bmpyr][DCA] states at low energy.

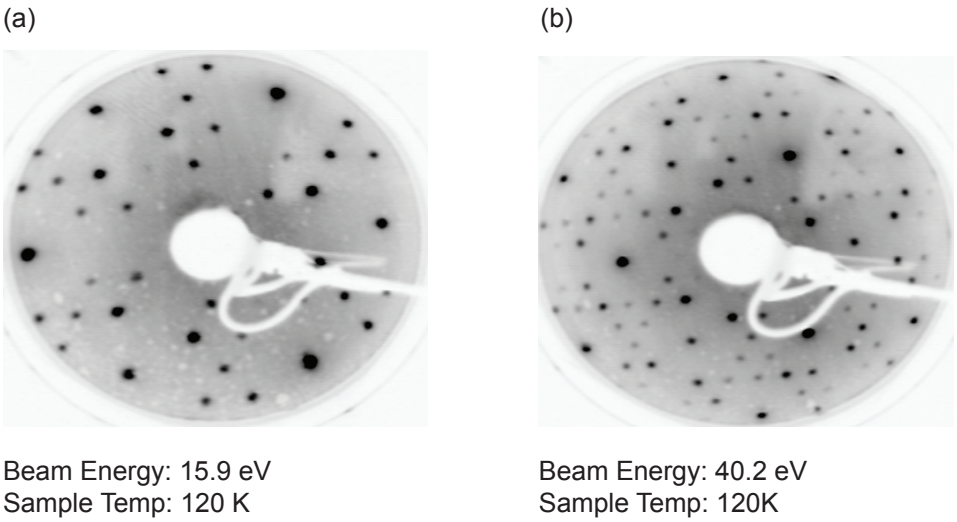

Figure 5.2: LEED images of ∼1 ML [Bmpyr][DCA].

The results presented in Figure 5.1 confirm that a monolayer of the RTIL grows in approximately 20 minutes under the present dosing conditions. At the top of the figure, low dosing times are plotted and the spectra are dominated by the surface states of Ag(111). As dosing time is increased, these electronic states intrinsic to the bare metal surface are slowly attenuated, and new states at lower energies begin to grow in. These emerging states come from the formation of the RTIL film, and the point at which these RTIL states begin to dominate the spectra is a dosing time of around 20 minutes.

5.3 Film Structure and Degradation

The studies of [Bmpyr][NTf_2] films, presented in the previous chapter, describe the degradation of films and outline a few mechanisms by which this degradation process could occur. In those studies, degradation was primary described by observing qualitative changes in the ultrafast dynamics of surface electronic states. Measurement of the structure of [Bmpyr][NTf_2] films using LEED was attempted multiple times, as it is known that [Bmpyr][NTf_2] crystallizes well above 120 K [11]. No LEED spots were observed for [Bmpyr][NTf_2] films at 120 K; the inability to measure a LEED signal is likely a consequence of the films degrading under electron flux.

In the case of [Bmpyr][DCA] films, a LEED pattern was successfully measured at a film temperature of 120 K. Two example images are presented in Figure 5.2, and show that the [Bmpyr][DCA] films form a crystalline structure that does not degrade in the presence of low energy electrons. A difference with respect to film degradation between [Bmpyr][NTf_2] and [Bmpyr][DCA] has been found for bulk systems using theoretical methods [95, 96]. The preliminary results presented here in the form of LEED spectra suggest that a similar difference holds when these two RTIL's are at a surface. This result is important because

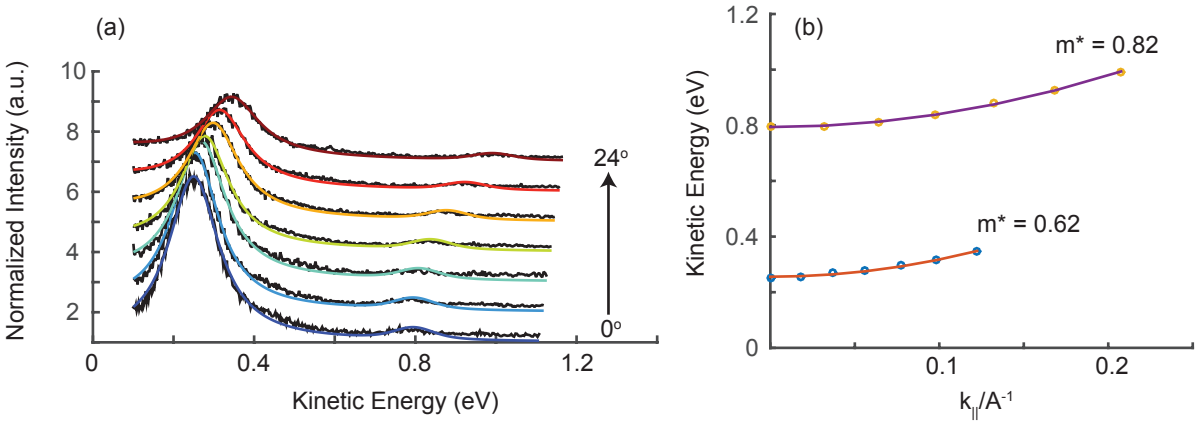

Figure 5.3: Dispersion measurements show that the two observable states in [Bmpyr][DCA] have IPS-like dispersive character. Pictured in (a) are data and corresponding energy-domain fits at angles between 0 and 24 degrees. Panel (b) shows the fits in k-space, and the fitted free-electron-like effective masses that describe these dispersive states.

it shows that simply changing the anion from $[NTf_2]^-$ to $[DCA]^-$ can fundamentally change the stability of a film, knowledge that is very useful in the context of incorporating RTIL's into devices.

5.4 Dispersion Characterization of Surface States

Two interfacial electronic states are observed in 1 ML [Bmpyr][DCA] films. Angle-resolved measurements reveal that both states have delocalized, free-electron-like character in the plane of the surface. Figure 5.3 shows spectra collected at a series of sample-detector angles (panel (a)) and the corresponding dispersion relations in reciprocal space for the two observed states (panel (b)). The very light (< 1 m_e) effective masses observed for both of these states suggest that they may be image potential states of the RTIL film itself. It is important to note that the bias between sample and detector was not carefully calibrated for these preliminary data, a bias of approximately -0.4 V was used. The effect of an incorrect bias is to change the observed kinetic energies, leading to a quantitatively incorrect values for dispersion relations and m* values. Nevertheless, there is a precedent for assignment of these states as members of an IPS series based on qualitative inspection of the data. Furthermore, an IPS hybrid state was observed as a precursor to solvation in [Bmpyr][NTf_2] films, so it is reasonable to expect the presence of a similar state in the present film of [Bmpyr][DCA]. Finally, the pristine crystalline structure of [Bmpyr][DCA] films observed by LEED (Figure 5.2) would allow for observation of not just the first member of the IPS series, but higher lying states as well. The best assignment for the two states observed in the [Bmpyr][DCA] spectra is therefore the first two members of a film-based series of image states.

5.5 Dynamics

The results from angle-resolved measurements suggest that an IPS series is being observed in 1 ML [Bmpyr][DCA]films, and this assignment is further supported by time-resolved experiments. Figure 5.4(a) shows a false color contour plot of a dynamic scan of a 1 ML film of [Bmpyr][DCA]. There are 3 major features apparent in these spectra, their energetic positions and lifetimes strongly suggest that they are an IPS series. Figure 5.4(b) shows the TPPE spectrum at a single time delay, 266 fs, to more clearly display the n=1, n=2, and n=3 states. Finally, the temporal evolution of the population in each state is plotted in Figure 5.4(c). The population of each state was represented by integrating the counts in a $\sim 100meV$ window around the peak center, these windows are illustrated using dotted lines in Figures 5.4(a) and (b).

Qualitative inspection of the dynamic traces in Figure 5.4(c) confirm the identity of the observed states as members of an IPS series associated with the RTIL film. The lifetimes of these states appear to be longer than that of IPS over clean metal. For example, the n = 1 state (red trace) persists for $>$ 1 ps in the [Bmpyr][DCA]films. By comparison, an n = 1 state on clean Ag (111) has a lifetime ¡ 100 fs [72]. The increased lifetime of the image states in [Bmpyr][DCA]is likely due to the RTIL film acting as a tunneling barrier. This was also observed in the case of [Bmpyr][NTf_2], where changing film thickness significantly increased the lifetime of the states observed in that system. An interesting further experiment would be to perform film-thickness-dependent measurements for films of [Bmpyr][DCA], then compare the observed effects to the ones seen in films of [Bmpyr][NTf_2]. This study, along with other further experiments involving RTIL's, is proposed in the Future Directions chapter at the end of this dissertation.

In addition to the IPS series, there are signals in the spectra shown in Figure 5.4(a) whose intensity peaks around t = 750 fs. These 'ghost' peaks are the result of experimental error: they come from residual 800 nm light that was not properly filtered after the OPA. As described in the experimental section, spatial filters were incorporated after the OPA to remove light of unwanted wavelengths. In this particular case, the spatial filter was not oriented correctly, allowing 800 nm light to interact with the sample. This leakthrough phenomenon has been documented before as the cause of false positive signals with time delays of 500-800 fs[79] and can be easily avoided by better positioning of the spatial filter within the post-OPA compression system.

5.6 Conclusion

Film formation of [Bmpyr][DCA]was characterized using dose-dependent TPPE and TPD. Using these measurements, monolayer films were grown and shown to support an image potential state series. The assignment of these states as IPS's was made based on their dispersive character, short lifetime, and relative energetic positions. Furthermore, LEED measurements showed that [Bmpyr][DCA]forms a crystalline lattice at 128K, and is resistant

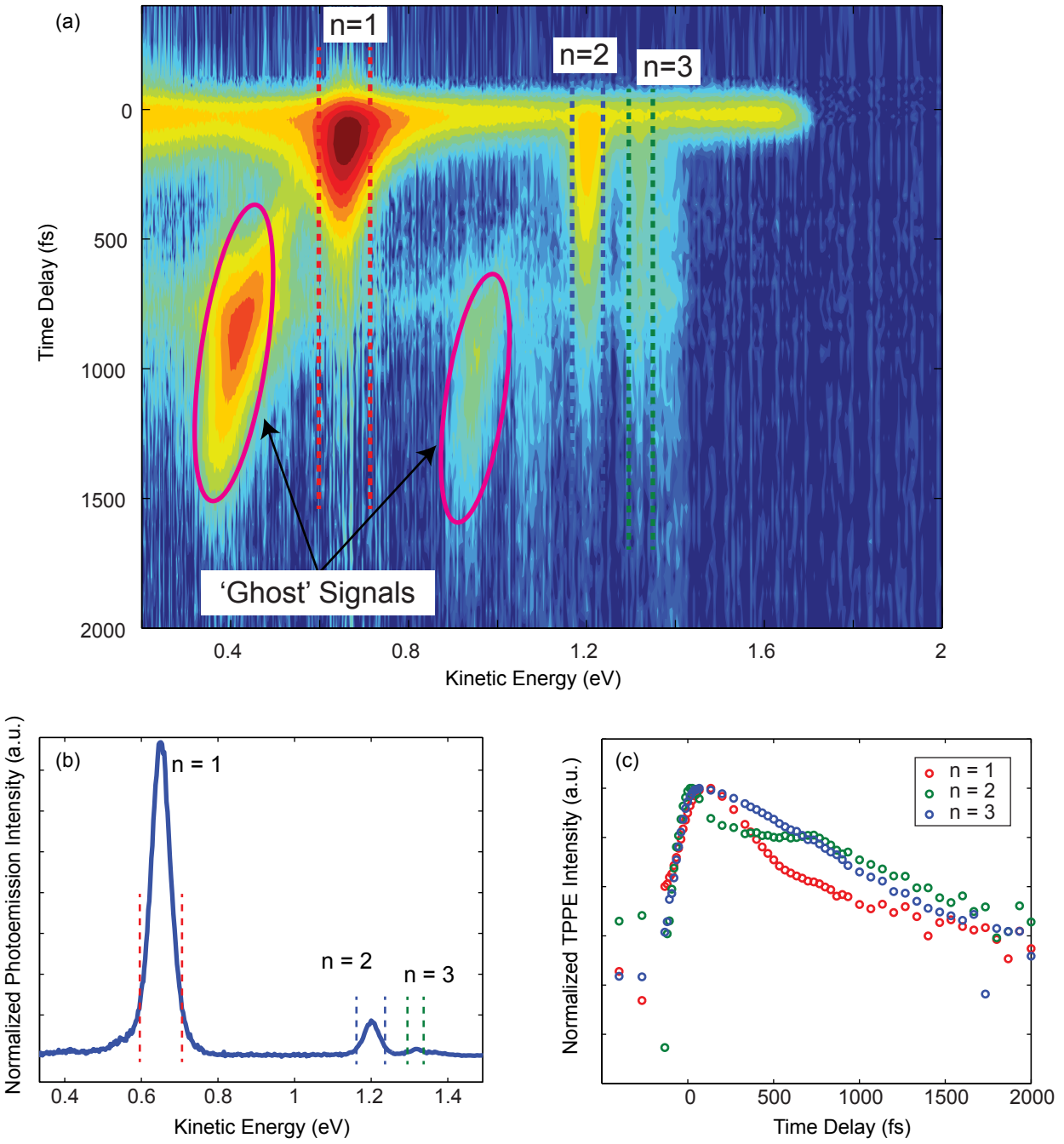

Figure 5.4: The dynamics of image states in [Bmpyr][DCA] are observed by taking time-resolved TPPE measurements of a 1 ML film. The false color contour plot in (a) shows the result of these time-resolved measurements. The n=1-3 image states are observed, as well as two 'ghost' signals that arise from erroneously unfiltered 800 nm light. To more easily see the IPS series, panel (b) shows the spectrum at a single time slice with no interference from ghost signals. The dotted lines enclosing each image state in (a) and (b) represent the integration window used to calculate the population dynamics shown in (c) on a normalized, log scale Y axis.

to degradation. The observation of LEED spots, lack of degradation, and presence of the first 3 members of an IPS series are all phenomena that were seen in [Bmpyr][DCA]but not observed in [Bmpyr][NTf_2]. Simply changing the identity of the anion, $[DCA]^-$ instead of $[NTf_2]^-$, was shown to dramatically change the nature of the physical structure and electronic states in an interfacial RTIL.

Chapter 6

Summary and Future Directions

6.1 Summary

The work presented in this dissertation focuses on documenting electronic states of device-relevant materials, characterizing the behavior of those states on the ultrafast timescale, and drawing conclusions and deeper physical insight based on the observed interfacial phenomena. Graphene and ionic liquids, the two main topics of study, are both classes of materials that are physically unique and hold much promise for improving modern electronic devices.

The graphene/SiC(0001) interface was shown to support an IPS series, both in the case of bilayer graphene (BLG) and corrugated buffer layer graphene. The characteristics (dispersion, lifetime, energetic position) of the IPS series were all the same within error for both forms of graphene, except in the case of the n = 3 lifetime which was significantly greater for BLG than it was for the buffer layer. The similarity between BLG and the buffer layer is evidence that the buffer layer is more graphene-like than previously expected, and gives rise to a surface potential equivalent to that of a free-standing graphene layer. This result is significant because of the importance of graphene in next-generation devices, and the role that the surface potential plays in the functioning mechanism of those devices.

The RTIL species [Bmpyr][NTf_2] and [Bmpyr][DCA] were both studied using TPD and TPPE techniques. Film formation was calibrated for both samples using dose-dependent TPPE and TPD, allowing the coverage to be precisely determined. In the case of [Bmpyr][NTf_2], an IPS-like delocalized precursor was observed to exist for ∼500 fs, after which the TPPE spectra were dominated by a solvated state. Changing film conditions allowed the energetic shift during solvation to be tuned between ∼300 meV and 1000 meV and the observable timescale of the solvation process to change from <0.5 ps to 195 ps. The results of Xe titration experiments suggest that the solvation process is oriented at the film/vacuum interface, and degradation observed on the ultrafast timescale points to radical anions being involved in solvation. No such degradation was observed for [Bmpyr][DCA] films, but a prisitine IPS series was found using TPPE. Low energy electron diffraction experiments showed that highly ordered crystalline films of [Bmpyr][DCA] can be formed by epitaxial dosing; this

crystalline structure is likely what allows the film to support an IPS series where high lying (n = 2+) states are clearly visible by TPPE.

6.2 Future Directions

One of the most exciting directions for future research is the exploration of more interfacial ionic liquids. As discussed at the end of Chapter 5, a simple substitution of anion was shown to drastically alter both the physical structure of an interfacial RTIL as well as change the nature of its surface states. While films of [Bmpyr][NTf_2] yielded an n =1 IPS precursor to a solvated state, [Bmpyr][DCA] films supported the first 3 states of an IPS series. The ability to resolve these states was likely due to the crystalline and degradation-resistant physical structure of the films of [Bmpyr][DCA], however surveying additional RTIL films could provide additional support of this explanation. Other open questions worth exploring include are how thicker films of [Bmpyr][DCA] behave, and whether solvation occurs at any coverage/temperature combination. A simple first step for future researchers would be to fully explore the behavior of [Bmpyr][DCA] by obtaining cleaner TPPE data at the correct grid bias and with proper filtering of residual 800 nm light. From there, coverages of $>$ 1ML [Bmpyr][DCA] could be investigated, as was done for [Bmpyr][NTf_2].

Ideally, a wide variety of interfacial ionic liquids would be studied to understand the differences in behavior between the different species, and ultimately link those behavioral dissimilarities to physical differences at the inter- and/or intra-molecular level. Degradation, observed for films of [Bmpyr][NTf_2] but not for [Bmpyr][DCA], would be an interesting first phenomenon to study. What properties determine whether or not an RTIL is susceptible to degradation? Do some films degrade faster than others and, if so, why are the rates different? Can solvation of excess charges occur in the absence of degradation, or is RTIL-based solvation intrinsically linked to intramolecular bond breaking? The answers to all of these questions would be interesting to the ionic liquid community, TPPE researchers, and important to understand in the context of device design. Furthermore, the majority of these inquiries could be addressed using the combination of TPPE, TPD, and LEED techniques whose power is demonstrated by the work presented in this dissertation. A final, more long-term goal would be to combine the graphene and RTIL projects into a single set of experiments: a study of RTIL behavior on a graphene substrate. Activated carbon and other carbon-rich electrodes are commonly used in devices because of their appropriate conductivity and high surface area. It would be very exciting to see how an RTIL behaves at such an interface; a simple first step would be to use bilayer or trilayer graphene as the substrate for RTIL growth. A trilayer of graphene would likely bear more structural similarity to the HOPG or activated carbon substrates used in electrochemical devices; it would be wise to begin this project by studying TL graphene/SiC (0001) in the absence of an RTIL overlayer. Directly studying ultrafast behavior of an RTIL/graphene interface would be both novel and directly relevant to device design, even more so than any other study proposed here.

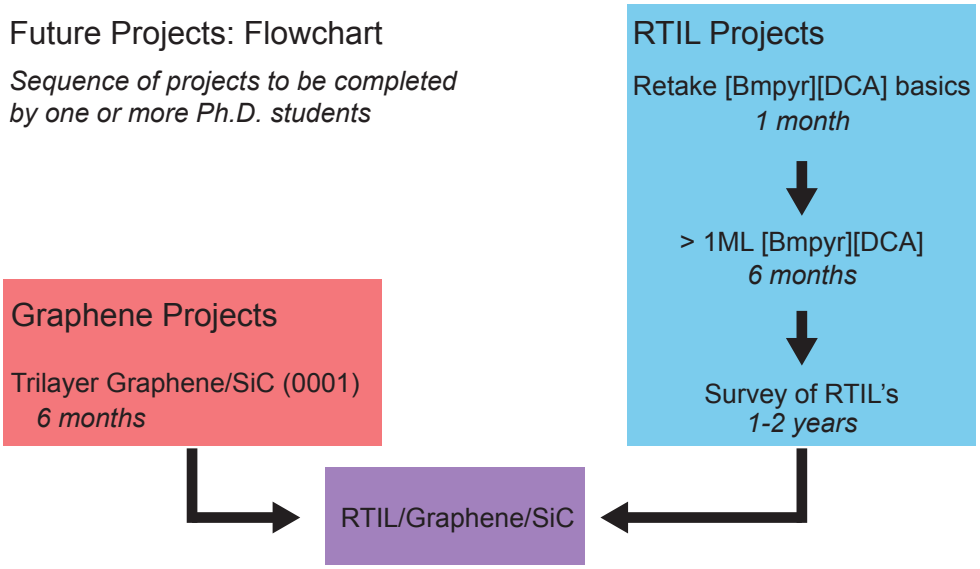

Figure 6.1: Flowchart of future projects that build upon the work presented in this dissertation. On the left are graphene-related projects, on the right are projects involving RTIL's, and in the middle is a final project combining the two materials.

The ideas outlined in this section are presented in the form of a flowchart in Figure 6.1. These projects could quite easily constitute the career of at least one Ph.D. student. Traditionally, such projects would be suggested to a younger member within the present research group. Unfortunately this is not an option, as I will be the last of professor Harris' students to graduate. My hope is that other groups with access to the appropriate laser and vacuum hardware will build upon the work presented in this dissertation and continue this exciting line of research. Understanding novel materials at interfaces may unlock the potential for safer and more effective devices, and the work presented herein is proof of how powerful the combination of TPPE and TPD can be in achieving that understanding.

Bibliography

[1] N. Armbrust, J. Güdde, P. Jakob, and U. Höfer. Time-Resolved Two-Photon Photoemission of Unoccupied Electronic States of Periodically Rippled Graphene on Ru(0001). *Phys. Rev. Lett.*, 108(5):1–5, January 2012.

[2] S. Arzhantsev, H. Jin, G. A. Baker, and M. Maroncelli. Measurements of the Complete Solvation Response in Ionic Liquids . *J. Phys Chem. B*, 111(18):4978–4989, May 2007.

[3] S. Arzhantsev, H. Jin, N. Ito, and M. Maroncelli. Observing the Complete Solvation Response of DCS in Imidazolium Ionic Liquids, from the Femtosecond to Nanosecond regimes. *Chem. Phys. Lett.*, 417(4-6):524–529, January 2006.

[4] R. Atkin, N. Borisenko, M. Drüschler, F. Endres, R. Hayes, B. Huber, and B. Roling. Structure and Dynamics of the Interfacial Layer Between Ionic Liquids and Electrode Materials. *J. Mol. Liq.*, 192:44–54, 2014.

[5] S. Baldelli. Surface Structure at the Ionic Liquid-Electrifed Metal Interface. *Acc. Chem. Res.*, 41(3):421–431, 2007.

[6] C. Berger, Z. Song, T. Li, X. Li, A. Y. Ogbazghi, R. Feng, Z. Dai, A. N. Marchenkov, E. H. Conrad, P. N. First, and W. A. de Heer. Ultrathin Epitaxial Graphite: 2D Electron Gas Properties and a Route toward Graphene-based Nanoelectronics. *J. Phys Chem. B*, 108(52):19912–19916, December 2004.

[7] L. Berthon, S. I. Nikitenko, I. Bisel, C. Berthon, M. Faucon, B. Saucerotte, N. Zorz, and P. Moisy. Influence of gamma irradiation on hydrophobic room-temperature ionic liquids [BuMeIm]PF6 and [BuMeIm](CF3SO2)2N. *J. Chem. Soc., Dalton Trans.*, (21):2526–2534, June 2006.

[8] Sangita Bose, Vyacheslav M Silkin, Robin Ohmann, Ivan Brihuega, Lucia Vitali, Christian H Michaelis, Pierre Mallet, Jean Yves Veuillen, M Alexander Schneider, Evgueni V Chulkov, Pedro M Echenique, and Klaus Kern. Image potential states as a quantum probe of graphene interfaces. *New Journal of Physics*, 12(2):023028, February 2010.

[9] U. Bovensiepen, C. Gahl, and M. Wolf. Solvation Dynamics and Evolution of the Spatial Extent of Photoinjected Electrons in D 2 O/Cu(111). *J. Phys Chem. B*, 107(33):8706–8715, August 2003.

[10] A. Brandt, S. Pohlmann, A. Varzi, A. Balducci, and S. Passerini. Ionic liquids in supercapacitors. *MRS Bull.*, 38(07):554–559, July 2013.

[11] F. Buchner, K. Forster-Tonigold, B. Uhl, D. Alwast, N. Wagner, H. Farkhondeh, A. Groß, and R. J. Behm. Toward the Microscopic Identification of Anions and Cations at the Ionic Liquid—Ag(111) Interface: A Combined Experimental and Theoretical Investigation. *ACS Nano*, 7(9):7773–7784, September 2013.

[12] Benjamin William Caplins. *Electronic Structure of the Metal/Phthalocyanine Interface Probed by Two-Photon Photoemission.* PhD thesis, University of California, Berkeley, 2015.

[13] J. R. Casey, R. E. Larsen, and B. J. Schwartz. Resonance Raman and Temperature-Dependent Electronic Absorption Spectra of Cavity and Noncavity Models of the Hydrated Electron. *PNAS*, 110(8):2712–7, 2013.

[14] E. W. Castner, C. J. Margulis, M. Maroncelli, and J. F. Wishart. Ionic Liquids: Structure and Photochemical Reactions. *Annu. Rev. Phys. Chem.*, 62:85–105, January 2011.

[15] E. W. Castner and J. F. Wishart. Spotlight on Ionic Liquids. *J. Chem. Phys.*, 132(12):120901, March 2010.

[16] E. W. Castner, J. F. Wishart, and H. Shirota. Intermolecular Dynamics, Interactions, and Solvation in Ionic Liquids. *Acc. Chem. Res.*, 40(11):1217–27, November 2007.

[17] N. Chandrasekhar, O. Schalk, and A. N. Unterreiner. Femtosecond UV Excitation in Imidazolium-based Ionic Liquids. *J. Phys Chem. B*, 112(49):15718–15724, 2008.

[18] X. Chen and S. E. Bradforth. The Ultrafast Dynamics of Photodetachment. *Annu. Rev. Phys. Chem.*, 59:203–231, 2008.

[19] T. Cremer, L. Wibmer, S. K. Calderón, A. Deyko, F. Maier, and H. P. Steinrück. Interfaces of Ionic Liquids and Transition Metal Surfaces-Adsorption, Growth, and Thermal Reactions of Ultrathin [C1C1Im][Tf2N] Films on Metallic and Oxidised Ni(111) Surfaces. *PCCP*, 14(15):5153–63, April 2012.

[20] A. Deyko, T. Cremer, F. Rietzler, S. Perkin, L. Crowhurst, T. Welton, H.-P. Steinruck, and F. Maier. Interfacial Behavior of Thin Ionic Liquid Films on Mica. *J. Phys. Chem. C*, 117(10):5101–5111, 2013.

[21] M. J. Earle, P. B. Mccormac, and K. R. Seddon. Diels - Alder Reactions in Ionic Liquids a Safe Recyclable Alternative to Lithium Perchlorate - Diethyl Ether Mixtures. *Green Chem.*, 1(1):23–25, 1999.

[22] B. Efron and R.J. Tibshirani. *An Introduction to the Bootstrap*. Chapman and Hall, New York, 1993.

[23] M. H. Elkins, H. L. Williams, A. T. Shreve, and D. M. Neumark. Relaxation Mechanism of the Hydrated Electron. *Science*, 342(6165):1496–1499, December 2013.

[24] V. N. Emel'yanenko, S. P. Verevkin, A. Heintz, J. A. Corfield, A. Deyko, K. R. J. Lovelock, P. Licence, and R.G. Jones. Pyrrolidinium-based Ionic Liquids. 1-butyl-1-methyl Pyrrolidinium Dicyanoamide: Thermochemical Measurement, Mass Spectrometry, and ab initio Calculations. *J. Phys Chem. B*, 112(37):11734–11742, 2008.

[25] K. V. Emtsev, F. Speck, Th. Seyller, and L. Ley. Interaction, Growth, and Ordering of Epitaxial Graphene on SiC{0001} Surfaces: A Comparative Photoelectron Spectroscopy Study. *Phys. Rev. B*, 77(15):1–10, April 2008.

[26] F. Endres. Physical Chemistry of Ionic Liquids. *PCCP*, 12(8):1648, February 2010.

[27] M. V. Fedorov and A. A. Kornyshev. Ionic Liquids at Electrified Interfaces, 2014.

[28] El. Frackowiak, G. Lota, and J. Pernak. Room-temperature Phosphonium Ionic Liquids for Supercapacitor Application. *App. Phys. Lett.*, 86(16):164104, 2005.

[29] A. M. Funston, T. A. Fadeeva, J. F. Wishart, and E. W. Castner. Fluorescence Probing of Temperature-dependent Dynamics and Friction in Ionic Liquid Local Environments. *J. Phys Chem. B*, 111(18):4963–4977, 2007.

[30] N. Garcia, B. Reihl, K. Frank, and A. Williams. Image States: Binding Energies, Effective Masses, and Surface Corrugation. *Phys. Rev. Lett.*, 54(6):591–594, February 1985.

[31] S. Goler, C. Coletti, P. Pingue, F. Colangelo, V. Pellegrini, K. V. Emtsev, S. Forti, U. Starke, F. Beltram, and S. Heun. Revealing the Atomic Structure of the Buffer Layer Between SiC(0001) and Epitaxial Graphene. *Carbon*, 51(0001):249–254, January 2013.

[32] J. Grodkowski and P. Neta. Formation and reaction of Br2 - Radicals in the Ionic Liquid Methyltributylammonium Bis(trifluoromethylsulfonyl)imide and in Other Solvents. *J. Phys. Chem. A*, 106(46):11130–11134, 2002.

[33] J. P. Hallett and T. Welton. Room-temperature Ionic Liquids: Solvents for Synthesis and Catalysis. 2, 2011.

[34] P. Hapiot and C. Lagrost. Electrochemical Reactivity in Room-Temperature Ionic Liquids. *Chem. Rev.*, 108(7):2238–2264, July 2008.

[35] N. A. W. Holzwarth, S. G. Louie, and S. Rabii. X-ray Form Factors and the Electronic Structure of Graphite. *Phys. Rev. B*, 26(10):5382–5390, November 1982.

[36] M. L. Horng, J. A. Gardecki, A. Papazyan, and M. Maroncelli. Subpicosecond Measurement of Polar Solvation Dynamics: {Coumarin} 153 Revisited. *J. Phys. Chem.*, 99:17311, 1995.

[37] J. A. Ingram, R. S. Moog, N. Ito, R. Biswas, and M. Maroncelli. Solute Rotation and Solvation Dynamics in a Room-Temperature Ionic Liquid. *J. Phys Chem. B*, 107:5926–5932, 2003.

[38] M. Ishikawa, T. Sugimoto, M. Kikuta, E. Ishiko, and M. Kono. Pure Ionic Liquid Electrolytes Compatible with a Graphitized Carbon Negative Electrode in Rechargeable Lithium-ion Batteries. *J.of Power Sources*, 162(1):658–662, November 2006.

[39] H. Jin, G. A. Baker, S. Arzhantsev, J. Dong, and M. Maroncelli. Solvation and Rotational Dynamics of Coumarin 153 in Ionic Liquids: Comparisons to Conventional Solvents. *J. Phys Chem. B*, 111:7291–7302, 2007.

[40] P. Jungwirth and D. J. Tobias. Specific Ion Effects at the Air/water Interface, 2006.

[41] R. Katoh, Y. Yoshida, Y. Katsumura, and K. Takahashi. Electron Photodetachment from Iodide in Ionic Liquids Through Charge-Transfer-to-solvent Band Excitation. *J. Phys Chem. B*, 111(18):4770–4774, 2007.

[42] J. A. Kellar, J. M. P. Alaboson, Q. H. Wang, and M. C. Hersam. Identifying and Characterizing Epitaxial Graphene Domains on Partially Graphitized SiC(0001) Surfaces using Scanning Probe Microscopy. *App. Phys. Lett.*, 96(14):143103, 2010.

[43] R. Kundu, P. Mishra, B.R. Sekhar, M. Maniraj, and S.R. Barman. Electronic Structure of Single Crystal and Highly Oriented Pyrolytic Graphite from ARPES and KRIPES. *Physica B*, 407(5):827–832, March 2012.

[44] R. Laenen, T. Roth, and A. Laubereau. Novel Precursors of Solvated Electrons in Water: Evidence for a Charge Transfer Process. *Phys. Rev. Lett.*, 85:50–53, 2000.

[45] T. A. Land, T. Michely, R. J. Behm, J. C. Hemminger, and G. Comsa. STM Investigation of Single Layer Graphite Structures Produced on Pt(111) by Hydrocarbon Decomposition. *Surf. Sci.*, 264(3):261–270, March 1992.

[46] P. Lauffer, K. V. Emtsev, R. Graupner, Th. Seyller, and L. Ley. Atomic and Electronic Structure of Few-layer Graphene on SiC(0001) Studied with Scanning Tunneling Microscopy and Spectroscopy. *Phys. Rev. B*, 77(15):1–10, April 2008.

[47] G. Le Rouzo, C. Lamouroux, V. Dauvois, A. Dannoux, S. Legand, D. Durand, P. Moisy, and G. Moutiers. Anion Effect on Radiochemical Stability of Room-temperature Ionic Liquids under Gamma Irradiation. *J. Chem. Soc., Dalton Trans.*, (31):6175–84, August 2009.

[48] A. Lewandowski and A. Świderska Mocek. Ionic liquids as Electrolytes for Li-ion Batteries-An Overview of Electrochemical Studies. *J. Power Sources*, 194(2):601–609, December 2009.

[49] R. L. Lingle, N.-H. Ge, R. E. Jordan, J. D. McNeill, and C. B. Harris. Femtosecond Studies of Electron Tunneling at Metal-Dielectric Interfaces, 1996.

[50] K. R. J. Lovelock, I. J. Villar-Garcia, F. Maier, H. P. Steinrück, and P. Licence. Photoelectron Spectroscopy of Ionic Liquid-based Interfaces. *Chem. Rev.*, 110(9):5158–5190, 2010.

[51] M. Mezger, H. Schröder, H. Reichert, S. Schramm, J. S. Okasinski, S. Schöder, V. Honkimäki, M. Deutsch, B. M. Ocko, J. Ralston, M. Rohwerder, M. Stratmann, and H. Dosch. Molecular Layering of Fluorinated Ionic Liquids at a Charged Sapphire (0001) Surface. *Science*, 322(5900):424–428, 2008.

[52] A. D. Miller, I. Bezel, K. J. Gaffney, S. Garrett-Roe, S. H. Liu, P. Szymanski, and C B Harris. Electron Solvation in Two Dimensions. *Science*, 297(5584):1163–6, August 2002.

[53] F. Molins I Domenech, B. FitzPatrick, A. T. Healy, and D. A. Blank. Photodetachment and Electron Reactivity in 1-methyl-1-butyl-pyrrolidinium bis(trifluoromethylsulfonyl)amide. *J. Chem. Phys.*, 137(3):034512, July 2012.

[54] J. S. Moon, D. Curtis, D. Zehnder, S. Kim, D. K. Gaskill, G. G. Jernigan, R. L. Myers-Ward, C. R. Eddy, P. M. Campbell, K. M. Lee, and P. Asbeck. Low-phase-noise Graphene FETs in Ambipolar RF Applications. *Elec. Dev. Lett.*, 32(3):270–272, 2011.

[55] E. A. Muller, M. L. Strader, J. E. Johns, A. Yang, B. W. Caplins, A. J. Shearer, D. E. Suich, and C. B. Harris. Femtosecond Electron Solvation at the Ionic Liquid/Metal Electrode Interface. *JACS*, 135(29):10646–53, July 2013.

[56] M. Muntwiler and X.-Y. Zhu. Formation of Two-Dimensional Polarons that are Absent in Three-Dimensional Crystals. *Physical Review Letters*, 98(24):246801, June 2007.

[57] A. Nagashima, K. Nuka, H. Itoh, T. Ichinokawa, C. Oshima, and S. Otani. Electronic States of Monolayer Graphite Formed on TiC(111) Surface. *Surf. Sci.*, 291(1-2):93–98, July 1993.

[58] D. Niesner, Th. Fauster, J. Dadap, N. Zaki, K. Knox, P.-C. Yeh, R. Bhandari, R. Osgood, M. Petrović, and M. Kralj. Trapping Surface Electrons on Graphene Layers and Islands. *Phys. Rev. B*, 85(8):1–5, February 2012.

[59] D. Nobis, M. Potenz, D. Niesner, and T. Fauster. Image-potential States of Graphene on Noble-metal Surfaces. *Phys. Rev. B*, 88(19):195435, November 2013.

[60] Md.W.K. Nomani, R. Shishir, M. Qazi, D. Diwan, V. B. Shields, M. G. Spencer, G. S. Tompa, N. M. Sbrockey, and G. Koley. Highly Sensitive and Selective Detection of NO2 using Epitaxial Graphene on 6H-SiC. *Sens. Actuators, B*, 150(1):301–307, September 2010.

[61] K S Novoselov, A K Geim, S V Morozov, D Jiang, M I Katsnelson, I V Grigorieva, S V Dubonos, and A A Firsov. Two-dimensional gas of massless Dirac fermions in graphene. *Nature*, 438(7065):197–200, November 2005.

[62] K. S. Novoselov, A. K. Geim, S. V. Morozov, D. Jiang, Y. Zhang, S. V. Dubonos, I V Grigorieva, and a a Firsov. Electric Field Effect in Atomically Thin Carbon Films. *Science*, 306(5696):666–9, October 2004.

[63] U. Novoselov, K.S.; Jiang, Z.; Zhang, Y.; Morozov, S.V.; Stormer, H.L.; Zeitler. Room-Temperature Quantum Hall Effect in Graphene. *Science*, 315(5817):1379, 2007.

[64] R. Pearce, T. Iakimov, M. Andersson, L. Hultman, A. L. Spetz, and R. Yakimova. Epitaxially Grown Graphene Based Gas Sensors for Ultra Sensitive NO2 Detection. *Sens. Actuators, B*, 155(2):451–455, July 2011.

[65] H. Petek and S. Ogawa. Femtosecond Time-resolved Two-photon Photoemission Studies of Electron Dynamics in Metals, 1997.

[66] N. V. Plechkova and K. R. Seddon. Applications of Ionic Liquids in the Chemical Industry. *Chem. Soc. Rev.*, 37(1):123–50, January 2008.

[67] S. Reich, J. Maultzsch, C. Thomsen, and P. Ordejón. Tight-binding Description of Graphene. *Phys. Rev. B*, 66(3):035412, July 2002.

[68] F. W. Richey, C. Tran, V. Kalra, and Y. A. Elabd. Ionic Liquid Dynamics in Nanoporous Carbon Nanofibers in Supercapacitors Measured with in Operando Infrared Spectroelectrochemistry. *J. Phys. Chem. C*, 118(38):21846–21855, August 2014.

[69] C. Riedl, C. Coletti, and U. Starke. Structural and Electronic Properties of Epitaxial Graphene on SiC(0 0 0 1): a Review of Growth, Characterization, Transfer Doping and Hydrogen Intercalation. *J. Phys. D: Appl. Phys.*, 43(37):374009, September 2010.

[70] C. Riedl and U. Starke. Structural Properties of the Graphene-SiC(0001) Interface as a Key for the Preparation of Homogeneous Large-terrace Graphene Surfaces. *Phys. Rev. B*, 76(24):1–8, December 2007.

[71] F. Schedin, A. K. Geim, S. V. Morozov, E. W. Hill, P. Blake, M. I. Katsnelson, and K. S. Novoselov. Detection of Individual Gas Molecules Adsorbed on Graphene. *Nat. Mater.*, 6(9):652–5, September 2007.

[72] R. W. Schoenlein, J. G. Fujimoto, G. L. Eesley, and T. W. Capehart. Femtosecond Relaxation Dynamics of Image-Potential States. *Phys. Rev. B*, 43(6):4688–4698, February 1991.

[73] X. Shi, F. H. Long, H. Lu, and K. B. Eisenthal. Electron Solvation in Neat Alcohols. *J. Phys. Chem.*, 99:6917–6922, 1995.

[74] Y. Shim, J. Duan, M. Y. Choi, and H. J. Kim. Solvation in Molecular Ionic Liquids. *J. Chem. Phys.*, 119(13):6411, 2003.

[75] I. A. Shkrob, S. D. Chemerisov, and J. F. Wishart. The Initial Stages of Radiation Damage in Ionic Liquids and Ionic Liquid-Based Extraction Systems. *J. Phys Chem. B*, 111(40):11786–11793, 2007.

[76] Ilya A Shkrob, Timothy W Marin, Sergey D Chemerisov, and James F Wishart. Radiation induced redox reactions and fragmentation of constituent ions in ionic liquids. 1. Anions. *Journal of Physical Chemistry B*, 115(14):3872–3888, 2011.

[77] K. R. Siefermann, Y. Liu, E. Lugovoy, O. Link, M. Faubel, U. Buck, B. Winter, and B. Abel. Binding Energies, Lifetimes and Implications of Bulk and Interface Solvated Electrons in Water. *Nature Chem.*, 2(4):274–9, April 2010.

[78] V. Silkin, J. Zhao, F. Guinea, E. Chulkov, P. Echenique, and H. Petek. Image Potential States in Graphene. *Phys. Rev. B*, 80(12):1–4, September 2009.

[79] Budi Soediono. *Ultrafast Electron Dynamics of Ultrathin Films of Electrochemical Solvents Adsorbed on an Ag(111) Substrate*. PhD thesis, 2008.

[80] T. Someya, H. Fukidome, Y. Ishida, R. Yoshida, T. Iimori, R. Yukawa, K. Akikubo, Sh. Yamamoto, S. Yamamoto, T. Yamamoto, T. Kanai, K. Funakubo, M. Suemitsu, J. Itatani, F. Komori, S. Shin, and I. Matsuda. Observing Hot Carrier Distribution in an n-type Epitaxial Graphene on a SiC Substrate. *App. Phys. Lett.*, 104(16):161103, April 2014.

[81] J. Stähler, J.-C. Deinert, D. Wegkamp, S. Hagen, and M. Wolf. Real-Time Measurement of the Vertical Binding Energy during the Birth of a Solvated Electron. *JACS*, (i):150130121905001, 2015.

[82] J. Stähler, C. Gahl, U. Bovensiepen, and M. Wolf. Ultrafast Electron Dynamics at Ice-Metal Interfaces: Competition Between Heterogeneous Electron Transfer and Solvation. *J. Phys Chem. B*, 110(19):9637–44, May 2006.

[83] J. Stähler, M. Mehlhorn, U. Bovensiepen, M. Meyer, D. O. Kusmierek, K. Morgenstern, and M. Wolf. Impact of Ice Structure on Ultrafast Electron Dynamics in D2O Clusters on Cu(111). *Phys. Rev. Lett.*, 98(May):3–6, 2007.

[84] J. Stähler, M. Meyer, D. O. Kusmierek, U. Bovensiepen, and M. Wolf. Ultrafast Electron Transfer Dynamics at NH3/Cu(111) Interfaces: Determination of the Transient Tunneling Barrier. *JACS*, 130(27):8797–803, July 2008.

[85] Julia Stähler. *Freezing Hot Electrons*. PhD thesis, Freien Universitat Berlin, 2007.

[86] X. Sun, H. Luo, and S. Dai. Ionic Liquids-Based Extraction: a Promising Strategy for the Advanced Nuclear Fuel Cycle. *Chem. Rev.*, pages 2100–2128, 2011.

[87] K. Takahashi, J. Azuma, and M. Kamada. Two-dimensional Band Dispersion and Momentum-Resolved Lifetime of the Image-Potential State on Graphite Studied by Angle-Resolved Multiphoton Photoemission Spectroscopy. *Phys. Rev. B*, 85(7):075325, February 2012.

[88] K. Takahashi, M. Imamura, I. Yamamoto, J. Azuma, and M. Kamada. Image Potential States in Monolayer, Bilayer, and Trilayer Epitaxial Graphene Studied with Time- and Angle-Resolved Two-Photon Photoemission Spectroscopy. *Phys. Rev. B*, 89(15):155303, April 2014.

[89] K. Takahashi, K. Suda, T. Seto, Y. Katsumura, R. Katoh, R. A. Crowell, and J. F. Wishart. Photo-Detrapping of Solvated Electrons in an Ionic Liquid. *Radiat. Phys. Chem.*, 78(12):1129–1132, December 2009.

[90] L. Turi and P. J. Rossky. Theoretical Studies of Spectroscopy and Dynamics of Hydrated Electrons. *Chem. Rev.*, 112:5641–5674, 2012.

[91] Paul Walden. Molecular Weights and Electrical Conductivity of Several Fused Salts. *Bull Acad Imper Sci*, pages 405–422, 1914.

[92] R. Wen, B. Rahn, and O.M. Magnussen. Potential-Dependent Adlayer Structure and Dynamics at the Ionic Liquid/Au(111) Interface: A Molecular-Scale In Situ Video-STM Study. *Angew. Chem. Int. Ed.*, 2:n/a–n/a, 2015.

[93] M. Wiets, M. Weinelt, and T. Fauster. Electronic Structure of SiC(0001) Surfaces Studied by Two-Photon Photoemission. *Phys. Rev. B*, 68(12):1–11, September 2003.

[94] J. F. Wishart and I. A. Shkrob. The Radiation Chemistry of Ionic Liquids and its Implications for their Use in Nuclear Fuel Processing. In *Ionic Liquids: From Knowledge to Application*, pages 119–134. 2009.

[95] C. Xu, A. Durumeric, H. K. Kashyap, J. J. Kohanoff, and C. J. Margulis. Dynamics of Excess Electronic Charge in Aliphatic Ionic Liquids Containing the Bis(trifluoromethylsulfonyl)amide Anion. *JACS*, October 2013.

[96] C. Xu and C. J. Margulis. Solvation of an Excess Electron in Pyrrolidinium Dicyanamide Based Ionic Liquids. *J. Phys Chem. B*, 119(2):532–542, 2015.

[97] Changhui Xu, Aleksander Durumeric, Hemant K Kashyap, Jorge Kohanoff, and Claudio J Margulis. Dynamics of excess electronic charge in aliphatic ionic liquids containing the bis(trifluoromethylsulfonyl)amide anion. *Journal of the American Chemical Society*, 135(46):17528–17536, November 2013.

[98] Y. Yamamoto, Y. Suzuki, G. Tomasello, T. Horio, S. Karashima, R. Mitríc, and T. Suzuki. Time- and Angle-Resolved Photoemission Spectroscopy of Hydrated Electrons Near a Liquid Water Surface. *Phys. Rev. Lett.*, 112(18):187603, May 2014.

[99] Zhen Yang and Wubin Pan. Ionic Liquids: Green Solvents for Nonaqueous Biocatalysis. *Enzyme Microb. Technol.*, 37(1):19–28, June 2005.

[100] W. Yuan and G. Shi. Graphene-Based Gas Sensors. *J. Mater. Chem. A*, 1(35):10078, 2013.

[101] H. Zhao, S. Xia, and P. Ma. Use of Ionic Liquids as 'Green' Solvents for Extractions. *J. Chem. Technol. Biotechnol.*, 80(10):1089–1096, October 2005.

[102] F. Zhou, Y. Liang, and W. Liu. Ionic Liquid Lubricants: Designed Chemistry for Engineering Applications. *Chem Soc. Rev.*, 38(9):2590–2599, 2009.

Appendix A

Details of Coverage Calibration for [Bmpyr][NTf_2] Films

Temperature programmed desorption (TPD) and dose-dependent two-photon photoemission (TPPE) were used to calibrate film coverage. A m/z ratio of 84 was monitored in the TPD experiments, which corresponds to a major fragmentation peak of the $[Bmpyr]^+$ cation. The TPD results in A.1(b) show a multilayer peak at lower (∼400 K) temperatures and high dose times (>10 min) , while a monolayer peak grows in from 0-10 minutes at ∼470 K and effectively saturates. The inset of A.1(b) shows this behavior of monolayer and multilayer peaks: the area around each peak maximum is integrated and plotted as a function of dosing time. After 10 minutes of dosing, both the monolayer peak area saturates and the multilayer peak begins to grow in, implying that a monolayer is fully grown after 10 minutes of dosing. This conclusion is supported by the dose-dependent TPPE spectra in A.1(a), which show a shift in the RTIL peak's energy between 8 and 12 minutes of dosing. We therefore assign a dosing rate of 0.1 ML/min, which is used to calibrate all subsequent film growth.

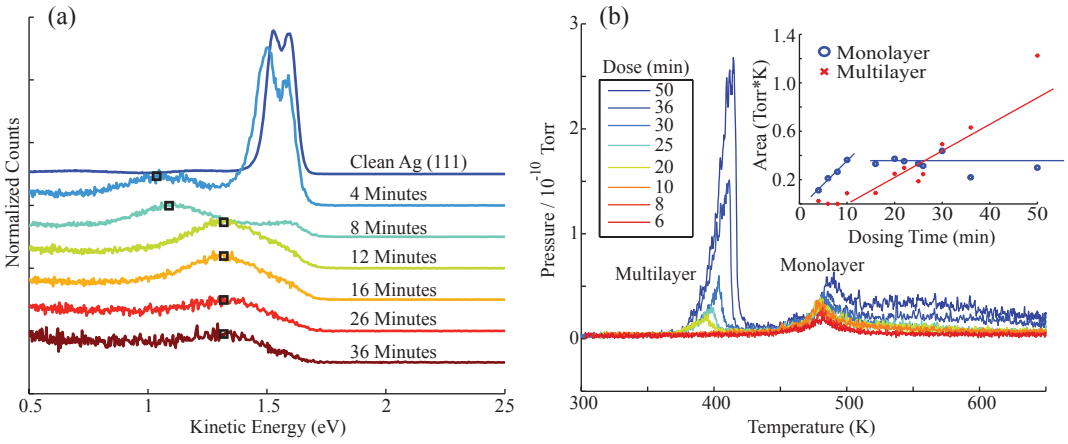

Figure A.1: Details of RTIL film Coverage Calibration

Appendix B

FIlm Photodegradation Measurements

As discussed in the main text, an electron excited from the Ag(111) substrate during the TPPE process is expected to perturb the local environment of the RTIL film. Our aim is to study the behavior of an excess electron in an initially unperturbed environment; we must therefore decide what the effect of the excess electron is and how long that effect takes to become significant. Our initial finding was that prolonged exposure to the laser beam on the 30 minute timescale resulted in a decrease in TPPE signal, and that this decrease in signal was more pronounced at longer time delays and in thicker films. We therefore decided to monitor the TPPE signal at a series of different time delays as a function of exposure time.

Since collection times for TPPE spectra are generally on the order of 30 s, we monitored change in intensity versus exposure on the single minute timescale. To approximate a zero-exposure case, the sample was continuously moved for the first scan at a given time delay, subsequent scans were taken every 5 s up to a maximum of 60 s. The relationship of solvated state intensity versus exposure time was linear in all cases, the slope at each delay time was found using a linear regression. Figure B.1 shows the final result of this set of experiments: the percent change in intensity per 15 s at several characteristic time delays for coverages of 1-3 ML. We present the percent change per 15 s because for all of the time-resolved data presented later in this study, each time slice was collected for 15 s. Immediately obvious from figure B.1 is that degradation becomes more of a problem as sample coverage is increased. The 1 ML spectra, seen most easily in B.1(a), decay by $< 2\%$ at all measured delays, while the 3 ML films decay by a more substantial 4-6%. The most significant result of the degradation experiments is that the absolute worst-case scenario of a thick film at a delay time of 200 ps shows a maximum change in signal of only 7% over the course of 15 s. We deemed a change of intensity less than 10% over the course of a collection to be acceptable, and therefore conclude that collection times of 15 s is a suitably conservative approach. During all subsequent time-resolved experiments, each time slice was collected for 15 s after which the sample was translated by 0.15 mm to give the $\sim$0.1 mm diameter laser spot a fresh area to interrogate.

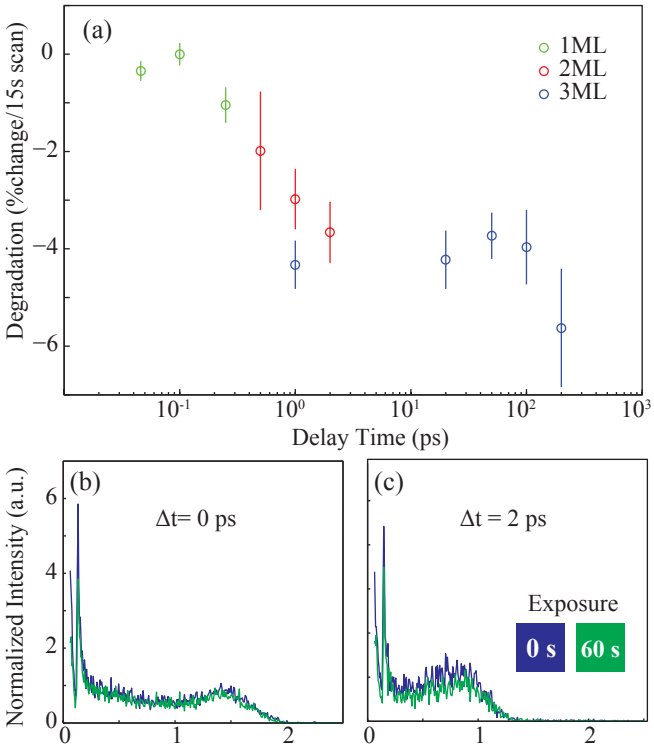

Figure B.1: Characterization of Ultrafast Photodegradation in [Bmpyr][NTf_2] Films

Appendix C

Multiexponential Fitting for [Bmpyr][NTf_2] Spectra

In order to convey the results of fitting time-dependent population data in a way that made it easy to compare films of different thickness and temperature, average lifetimes for each film were calculated. At film thicknesses of 1-3 ML, sums of 1-3 exponentials were used respectively to fit the change in peak intensity as a function of delay time:

$$I(t) = \sum_{i=1}^{N} a_i exp(-t/\tau_i) \tag{C.1}$$

T (K)	Cvg (ML)	A_1	T_1(fs)	A_2	T_2(fs)	A_3	T_3(fs)
300	1	2.31 ± 1.34	73 ± 20				
	2	1.03 ± 0.12	322 ± 20	0.33 ± 0.08	3244 ± 1073		
	3	0.54 ± 0.08	410 ± 110	0.42 ± 0.84	3205 ± 2217	0.25 ± 0.18	67233 ± 46727
130	1	2.64 ± 2.86	85 ± 20				
	2	0.54 ± 0.21	379 ± 143	0.68 ± 0.17	3291 ± 494		
	3	0.42 ± 0.25	376 ± 314	0.33 ± 0.29	22329 ± 32523	0.48 ± 0.24	208075 ± 81545

Table C.1: Parameters from Multiexponential Population Fits of RTIL Films

For each data set, the MATLAB software package was used to fit the appropriate exponential function. Table S1 shows the full set of fitting parameters for films of thickness 1-3 ML and temperature 300 K and 130 K. Each entry in this table is an average across multiple datasets corresponding to multiple, independently prepared films. The amplitudes and lifetimes for each film condition were combined into a single number that could represent population dynamics. The fractional contribution of each exponential component to the overall intensity is found by dividing the integral of the intensity for a given amplitude and lifetime by the total area under the decay curve:

$$f_i = \frac{a_i \tau_i}{\sum_{j=1}^{N} a_j \tau_j} \tag{C.2}$$

The average lifetime is then found by adding up each lifetime multiplied by its fractional contribution:

$$\tau_{avg} = \sum_{i=1}^{N} f_i \tau_i = \frac{\sum_{i=1}^{N} a_i \tau_i^2}{\sum_{j=1}^{N} a_j \tau_j} \tag{C.3}$$